Marine Geology 474 (2024) 107334

Contents lists available at ScienceDirect

Marine Geology

journal homepage: www.elsevier.com/locate/margo

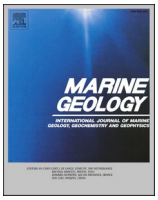

Identification of the Storegga event offshore Shetland

Jane L. Earland [a,*], James D. Scourse [a], Tobias Ehmen [a], Sev Kender [a], Philippa Ascough [b]

[a] Department of Earth and Environmental Science, University of Exeter Penryn Campus, Cornwall, UK
[b] NEIF Radiocarbon Laboratory, SUERC, Rankine Avenue, East Kilbride G75 0QF, United Kingdom

ARTICLE INFO

Editor: Michele Rebesco

Keywords:
Tsunamis and their deposits
Shelf processes
North Sea
Holocene

ABSTRACT

The Shetland Islands (UK) are a seminal location for investigating palaeo-tsunami deposits. Onshore evidence suggests three tsunami have occurred during the Holocene: the Storegga tsunami ca. 8150 cal yr BP, the Garth tsunami ca. 5500 cal yr BP and the Dury Voe tsunami ca. 1500 cal yr BP. However, little research has been published on the impact of tsunami on the subtidal shelf where a large amount of North Sea hydrocarbon infrastructure is located. Here, we test the hypothesis that Holocene tsunami impacted shelf sediments, using radiocarbon dating and sedimentological characterization of cores recovered from the Fetlar Basin, offshore east Shetland. The cores contain distinct sand and shell lenses within a Holocene mud sequence, indicating a sudden change in hydrodynamic conditions. Radiocarbon dates bracketing the sand lenses overlap with the published dates for the Storegga event. Dates within the deposit are older (>9 cal. yr BP) which is consistent with reworking and redeposition of earlier sediments. Particle size analysis, ITRAX and MSCL data evidence increases in mean grain size, a reduction in sorting capacity, increased shell concentrations and peaks in associated elements (log(Ca/Fe), log(Ca/Ti) and Sr). These attributes indicate transport of allochthonous material from the inner shelf, and are typical of tsunami backwash-generated submarine debris flows. No evidence was found within the cores for any later Holocene tsunami, which may be due to either bioturbation, active currents, or lack of an initial deposit. The disturbance of sediments, and generation of a submarine debris flow within the Fetlar Basin by the Storegga event highlights the need to assess the potential impact of any future tsunami on planned and existing infrastructure at seabed. Erosion and deposition of allochthonous older marine sediment by the Storegga event also has consequence for interpretation of the coeval 8.2 ka cold event in marine sedimentary records in the tsunami affected region.

1. Introduction

A key component of coastal hazard risk assessment is knowledge of the frequency and magnitude of past events (Evelpidou et al., 2022; Nott, 2003; Switzer et al., 2014). Whilst historical documents and instrumental data are useful tools for identifying relatively recent events, they cannot facilitate our understanding of hazards over greater time intervals. In tsunami research, palaeo-sedimentary archives such as onshore and offshore deposits can provide crucial insights into the age, recurrence rates and size of these events over geological time scales (Costa and Andrade, 2020; Dawson and Shi, 2000; De Martini et al., 2021; Engel et al., 2020; Garrett et al., 2018; Goff et al., 2012).

The Shetland Islands, situated 170 km north of mainland Scotland, have become an important location for identifying palaeo-tsunami in the North Sea region (Fig. 1). Onshore deposits suggests three tsunami have occurred during the Holocene: the Storegga tsunami ca. 8150 cal yr BP (Bondevik et al., 2003), the Garth tsunami ca. 5500 cal yr BP (Bondevik et al., 2005) and the Dury Voe tsunami ca. 1500 cal yr BP (Bondevik et al., 2005; Dawson et al., 2006; Engel et al., 2023). Deposits from these events are found in exposures of peat, boreholes and lake sediments, and are characterised as distinct layers of marine sand, wood fragments and rip-up clasts which fine inland (Bondevik et al., 2005; Bondevik et al., 2003; Bristow and Buck, 2021; Dawson et al., 2006; Engel et al., 2023).

The Storegga tsunami has been the primary focus for research on Shetland, evidence for which has also been found at coastal locations in Greenland (Wagner et al., 2007), the Faroe Islands (Grauert et al., 2001), western Norway (Bondevik et al., 1997; Rasmussen et al., 2018; Romundset and Bondevik, 2011) and mainland Scotland (Dawson et al., 1988; Dawson and Smith, 2000). The tsunami, discussed and summarised by Bondevik (2019), was triggered by a slip of 1300 to 2300 km^3 (Karstens et al., 2023) of sediment from the North Sea Fan in the Norwegian Sea called the Storegga Slide. Possible causes of the slide include

* Corresponding author.
E-mail address: je391@exeter.ac.uk (J.L. Earland).

https://doi.org/10.1016/j.margeo.2024.107334
Received 20 February 2024; Received in revised form 30 May 2024; Accepted 7 June 2024
Available online 17 June 2024

earthquake activity, melting of gas hydrates resulting from Northern Hemisphere deglaciation, or a combination of both (Bryn et al., 2005). On Shetland, the minimum run-up heights for Storegga have been estimated at 28.1–31.8 m (Dawson et al., 2020).

While onshore evidence is abundant, there is currently limited published evidence of the tsunami in offshore marine sequences around Shetland, or on the Northwest European continental shelf. During the SEACHANGE research cruise DY150 in early 2022, sediment cores were recovered offshore east Shetland from the Fetlar Basin. These cores contained distinct sand and shell lag lenses within a Holocene mud sequence, indicating increases in bed shear stress. Here, we test the hypothesis that these lenses represent the subtidal expression of a North Sea tsunami, based on radiocarbon dating, the defining sedimentary characteristics and geophysical profiles. Such findings may be important for understanding potential risks to extensive infrastructure at similar water depths around the North Sea Basin. They may also have implications for previous and future interpretations of the 8.2 ka cold event (Alley and Ágústsdóttir, 2005; Estrella-Martínez et al., 2019; Klitgaard-Kristensen et al., 1998; Rohling and Pälike, 2005) in marine sedimentary archives.

2. Regional setting

The Fetlar Basin is situated in the Northeast of the Shetland archipelago between Mainland, Yell, Whalsay and Fetlar (Fig. 1). Pleistocene deposits in this basin are some of the thickest in Shetland, consisting of grey till overlain by post-glacial soft muds containing high concentrations of hydrogen sulphide. In coastal locations, Holocene marine deposits consist of gravelly sands and shell-rich gravels, representing the abundance of marine fauna at these locations (Cox, 2021). Hydrocarbon (oil and gas) pipelines are present within the basin at 90 m water depth, and shallower depths as they pass into Yell Sound (Marine Scotland, 2019).

3. Methods

3.1. Core collection

Sediment cores DY150 FB A PC012 (60.504782°N, −0.941149°W), and DY150 FB A PC013 (60.504937°N, −0.941549°W) were collected in the Fetlar Basin using a NIOZ piston corer (Scourse et al., 2022). Both cores were collected from the same station (Fetlar Basin A), ~25 m apart, at 116 m present day water depth.

Cores were cut into 1 m sections onboard, split using a Geotek core

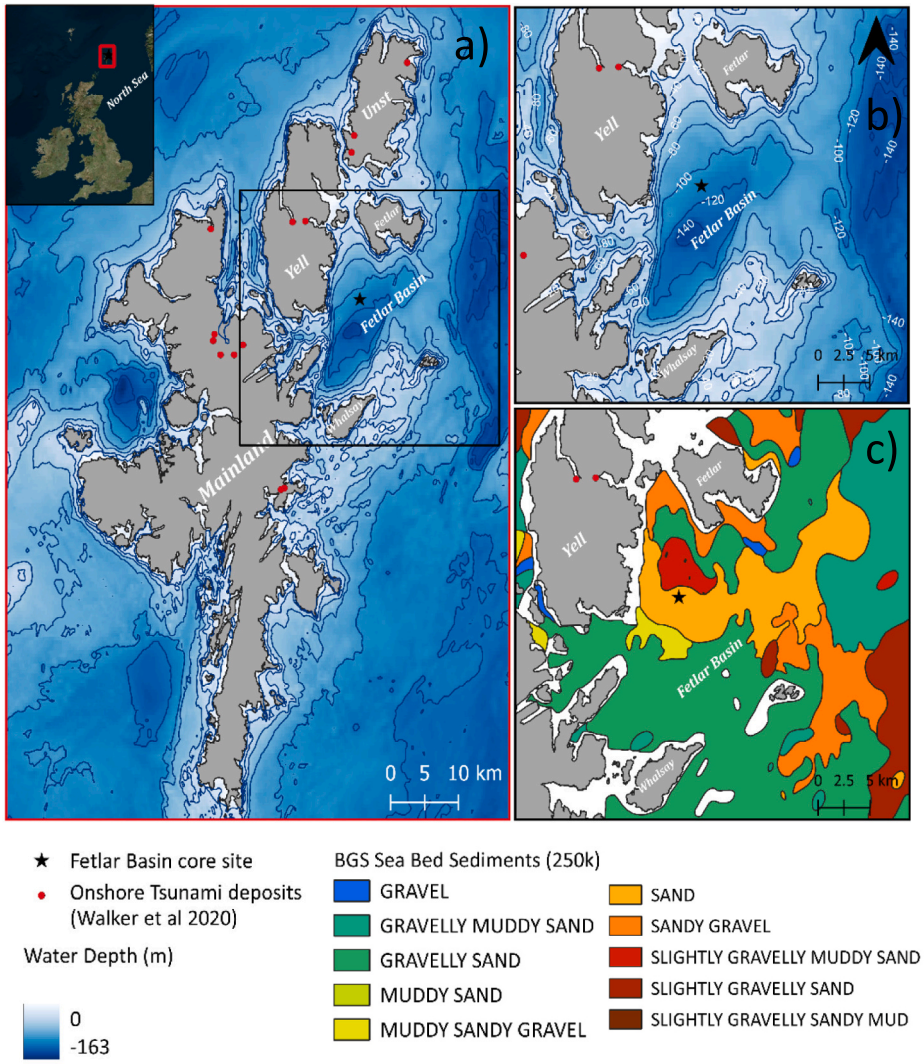

Fig. 1. (a,b) Fetlar Basin (Shetland) coring site. (c) BGS (250 k) seabed geology. Recorded onshore deposits from palaeo-tsunami (red dots) from Walker et al., (2020). (For interpretation of the references to colour in this figure legend, the reader is referred to the web version of this article.)

splitter and photographed. Visual core logging was completed to identify preliminary lithostratigraphic units, including the aforementioned lenses of shell rich sand.

3.2. Palaeo-water depth

Knowledge of the palaeo-water depth is crucial for understanding setting of the core site at the time of the Storegga event. For this study, a recently published interactive visualisation (PALTIDE), which integrates glacial isostatic adjustment and palaeo-tidal models, and allows relative sea level to be investigated at 1/12 degree resolution (Bradley et al., 2011; Scourse et al., 2024; Ward et al., 2016), was used to estimate the palaeo water-depth. Fig. 2 displays the palaeo-sea level curve for grid square 60.52 N,-0.92E, the closest data point to the Fetlar Basin coring site. These data suggest a RSL of −28.3 m at 8 ka, indicating a water depth of 87.7 m at the core site during Storegga event.

3.3. Physical properties

Physical properties data were obtained at the British Ocean Sediment Core Research Facility (BOSCORF) in Southampton. High resolution images and radiographic images were obtained using the Geotek MSCL-CIS (Multi Sensor Core Logging – Core Imaging System) and the Geotek ScoutXcan X-Ray Imaging Scanner. P-wave amplitude, P-wave velocity, Gamma Density and Electrical Resistivity were measured using the Geotek MSCL-S, fitted with a P-wave velocity sensor, gamma ray density meter and a non contact resistivity sensor. Magnetic susceptibility, greyscale reflectance, and CIELAB colour (L*, a*, b*) data were obtained using the Geotek MSCL-XYZ fitted with a Bartington magnetic susceptibility point sensor and a Konica Minolta spectrophotometer. The Cox Analytical Systems ITRAX X-ray Fluorescence (XRF), was used to produce elemental data. X-ray spectra were inspected and processed using Q-Spec version R15 software at BOSCORF. XRF data were treated and visualised using the open access R package itraxR (Bishop, 2022). Quality controlled data were plotted, and logarithmic ratios of elements computed. Data are displayed as counts per second. Further details on physical properties scanner set up can be seen in Appendix A.

3.4. Particle size analysis

Particle size analysis (PSA) was carried out on the full core length of PC012 at 16 cm resolution, and increased to 1 cm resolution 20 cm each side of the hypothesised tsunami deposit. PSA was performed at 20 cm each side the hypothesised tsunami deposit at 1 cm resolution in PC013. Analysis was carried out using a Malvern Mastersizer 3000 laser granulometry device, which has a measuring range of 0.01-3500 μm (Malvern Panalytical, 2024). Samples were oven dried at 40 °C, then mixed with 0.1% sodium hexametaphosphate (Calgon) solution. Samples were added to the dispersion unit of the Mastersizer and ultrasonically disaggregated for 30 s before measurement. GRADISTAT V.8 (Blott and Pye, 2001) was used to calculate statistical parameters, applying the programme's size scale which is based on Udden (1914) and Wentworth (1922). Skewness, sorting and kurtosis were calculated (Folk and Ward, 1957), and data were visualised in RStudio.

3.5. Sub-bottom profile/hydroacoustic survey

A Kongsberg SBP 27 sub-bottom profiler was used to acquire acoustic reflection data of the geological strata. Reflections occur where variations of acoustic impedance are present, which is the product of sound speed and density (Yilmaz, 1987). This makes sub-bottom profilers capable of detecting changes in physical properties that can be the result of changing sediment type.

Two-way travel time was converted to approximate depth using a sound velocity profile from CTD data for the water column and P-wave velocity from the geophysical core-logging of the core. Below 7 m core-logging data showed very low P-wave velocities of <500 m/s. We assume that this is incorrect due to the suggested P-wave velocity of continental shelf silty clays being 1519 m/s (Hamilton, 1971). This error is often caused by substandard contact between the sample and the P-wave sensors, and can occur in core sections where there is reduced water content (Webster et al., 2011). To correct this error, data were replaced with the average sound velocity value from 6 to 7 m for the purposes of depth conversion.

3.6. Radiocarbon dating

Samples for radiocarbon dating were selected in and surrounding the visually identified lenses of shelly sand rich material, in addition to other depths on the core to provide a general age-depth model. Dated carbonate consisted of mixed shell fragments, whole bivalve shells, or mixed benthic foraminifera. Where possible macrofossil shell samples were used, as these are suggested to be less affected by bioturbation (Heier-Nielsen et al., 1995). Additionally, previous work in northern Scotland indicates that there is no significant variation in the ^{14}C activity of different mollusc species, suggesting that using a mixture of bivalve species for dating is likely to have negligible impact on ^{14}C results (Ascough et al., 2005). For shell samples, the outer edge of the structure (representing the last growth of the organism) was used. The outer 20% by weight of all carbonate samples was removed by controlled acid

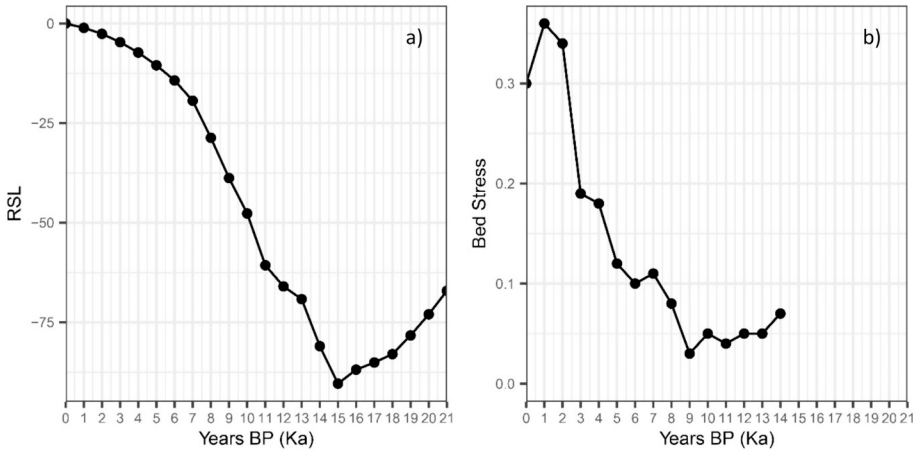

Fig. 2. Modelled (a) Relative Sea Level (RSL), (b) bed stress for grid square 60.52 N,-0.92E (the closest data point to the Fetlar Basin coring site) extracted from the interactive sea level tool PALTIDE (Bradley et al., 2011; Scourse et al., 2024; Ward et al., 2016).

hydrolysis to exclude surface contamination. The remaining sample carbonate was then completely hydrolysed to CO_2. The sample CO_2 was cryogenically purified before being reduced to graphite for measurement (Ascough et al., 2024). Accelerator mass spectrometry (AMS) radiocarbon (^{14}C) measurement was carried out at the Scottish Universities Environmental Research Centre NEIF Environmental Radiocarbon Laboratory (SUERC), and the Keck Carbon Cycle AMS Facility, University of California (UCAMS).

CALIB rev. 8 was used to calibrate ^{14}C measurements (Stuiver and Reimer, 1993), using the MARINE20 calibration curve (Heaton et al., 2020). A ΔR value of −109 ± 39 was used for all ^{14}C measurements, based on published values from Shetland (Cappelli and Austin, 2020; Reimer and Reimer, 2001). Despite the ΔR in the present study being derived from relatively modern material (1924), the ΔR is suggested to be relatively stable from ~5450–500 cal BP in northern Scotland (Russell et al., 2015), indicating that using a consistent ΔR is suitable for all mid-late Holocene ^{14}C ages. However, to account for some variability between published ΔR values in the region, a more cautious ΔR error of 2σ of the arithmetic mean was selected. Additionally, the ΔR chosen for this study closely aligns with values calculated in eastern Scotland for the Storegga event at −136 ± 44 (Rush et al., 2023). Differences between Rush et al.'s (2023) value and the value used here may be a result of spatial variation in ΔR. Although there may be some significant variability in ΔR values during the Younger Dryas (Austin et al., 2011), published local values for this period are unavailable, and hence the ΔR value used to calibrate these dates was the same as the Holocene ages in this study. A similar approach, using a consistent ΔR for late deglacial and Holocene marine sequences was used by Taylor et al. (2024) (ΔR of −126 ± 20) in north west Scotland.

3.7. Age models

Age models were generated using a Bayesian approach in rbacon version 3.1.1 (Blaauw and Christen, 2011). Coarse grained layers were classed as depositional events within the age model, due to the re-suspension and deposition of sediments, as in Hess et al. (2023). The model was computed using 4 cm thick sections and default prior distributions for shape and memory. The prior for the mean accumulation of rate was chosen at 20 cm/year based-on Bacon ballpark estimates. Default priors were used due to the absence of published accumulation rates in the region.

4. Results

4.1. Radiocarbon dating and age models

Results from radiocarbon dating are presented in Table 1, and age models in Fig. 3. In total five radiocarbon dates were omitted from the age model, one in PC012 four in PC013, due to the proposed hypothesis that older sediments and carbonate material were re-worked by the Storegga tsunami (see further detail in discussion below).

Table 1
Radiocarbon results.

Core	Publication Code	Sample depth (cm)	Material	Radiocarbon age (years BP)	Radiocarbon age 1σ uncertainty	Calibrated age range 95% (2σ) (cal yr BP)
DY150 FB A PC012	UCIAMS-281714	0.5	Shell fragments	440	35	Modern
DY150 FB A PC012	SUERC-108546	25.1	Single valve - *possibly A. islandica*	1548	37	896–1233
DY150 FB A PC012	UCIAMS-286683	159.5	Shell fragments	5568	32	5683 - 6078
DY150 FB A PC012	UCIAMS-281715	221.5	Shell fragments	7817	35	8035 - 8369
DY150 FB A PC012	UCIAMS-281716	224.5	Shell fragments	7873	35	8094 - 8429
DY150 FB A PC012	UCIAMS-281717	227.5	Shell fragments	10,256*	37	11,172 - 11,613
DY150 FB A PC012	UCIAMS-286684	230.5	Shell fragments	8077	33	8329 - 8681
DY150 FB A PC012	UCIAMS-286685	233.5	Shell fragments	8110	35	8357 - 8737
DY150 FB A PC012	UCIAMS-281718	320.5	Shell fragments	9170	37	9655 - 10,133
DY150 FB A PC012	SUERC-108547	463.7	Shell fragments	9967	40	10,751 - 11,184
DY150 FB A PC012	UCIAMS-286686	494.5	Shell fragments	10,120	40	10,989 - 11,400
DY150 FB A PC012	UCIAMS-286687	580.5	Shell fragments	10,558	37	11,567 - 12,101
DY150 FB A PC012	UCIAMS-286688	667.5	Mixed benthic foraminifera	12,320	52	13,591 - 14,033
DY150 FB A PC013	SUERC-108548	85.25	Single value - *Lucinoma borealis*	2885	35	2391 - 2759
DY150 FB A PC013	UCIAMS-286689	249.5	Shell fragments	8032*	35	8281 - 8619
DY150 FB A PC013	UCIAMS-286692	256.5	Shell fragments	8995*	35	9467 - 9864
DY150 FB A PC013	UCIAMS-281719	259.5	Shell fragments	8656*	35	9055 - 9436
DY150 FB A PC013	UCIAMS-281720	262.5	Shell fragments	9533*	37	10,185 - 10,561
DY150 FB A PC013	UCIAMS-281723	265.5	Shell fragments	7930	35	8169 - 8504
DY150 FB A PC013	SUERC-108549	480.5	Shell fragments	10,583	40	11,611 - 12,158

* Dates omitted from age model due to suspected reworking.

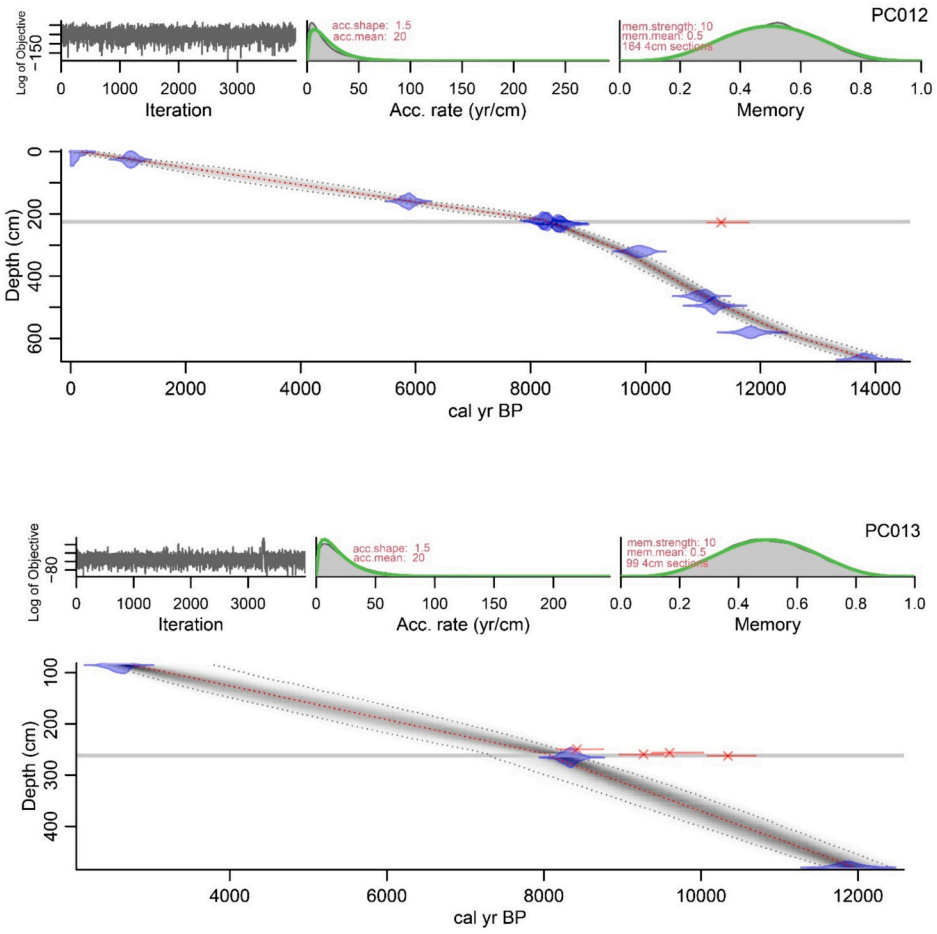

Fig. 3. Bayesian age-depth models produced using rbacon for PC012 (top) and PC013 (bottom). Red dotted line represents median modelled age, grey dotted line represents 2σ error range. Light grey horizontal bars represent deposits, modelled as slumps. Red horizontal lines with a cross represent ages excluded from age model due to suspected re-working within the deposit. (For interpretation of the references to colour in this figure legend, the reader is referred to the web version of this article.)

4.2. Sedimentary units

Results from physical properties and particle size analysis are presented in lithostratigraphic units. The unit boundaries are defined based on core PC012 and shown in Fig. 4, due to the availability of quantitative grain size data for the full core. XRF data and visual analysis indicated sedimentary units are very similar in PC013, although occur at slightly different depths due to local small-scale variation in sedimentation. Detailed plots of the shelly sandy lenses in both PC012 and PC013 are shown in Fig. 5 and Fig. 6.

4.2.1. Unit A

Unit A begins at the base of the core (767 cm), and comprises dark grey, poorly sorted coarse silt with mainly symmetrical and mesokurtic skewness. Some small white specks (assumed indistinguishable biogenic fragments) can be seen within the sediments. The mean grain size does not fluctuate significantly within this unit (average mean grain size 22.1 μm). This unit is differentiated from the unit above (B) due to the flecks of dark reddish brown and very dark grey, and higher magnetic susceptibility values, which reach 56×10^{-5} SI. X-radiographs reveal thick laminations and some whole bivalves. Elemental data show high Si, Ti, Fe and log(Si/Ca) values, and low log(Ca/Ti) and log(Ca/Fe) values. Approximate depth conversions from sub-bottom profiles indicate this unit is within a layer of homogenous material with few reflectors. There was insufficient carbonate material within this layer to yield a radiocarbon date.

4.2.2. Unit B

The base of Unit B (666 cm) is similar to Unit A in terms of grain size (coarse silt, average mean grain size 21.87 μm), sorting (poorly sorted), skewness (mainly symmetrical) and elemental properties. However, this unit is marked by much lower magnetic susceptibility values (15–20 $\times$ 10^{-5} SI) than Unit A, and a distinctly greyer colour without dark reddish-brown flecks. Radiocarbon dates the base of this unit to 13,591–14,033 cal BP (2σ).

4.2.3. Unit C

Unit C has a base at 580 cm, and is marked by a change in grain size to largely olive grey, very coarse, poorly sorted silt (average mean grain size 43.68 μm) sediments. The grain size distribution becomes more skewed, and sand content increases (41%) compared to Unit B. At the base of the section, the grain sizes are primarily trimodally distributed, and small whole bivalves as well as fragmented shells are present. Above this, the grain size distribution changes to include some poly- and bimodal distributions, and is unimodal by the top of the section. This unit has low magnetic susceptibility values. XRF data transition through the unit; upwards through the unit Si and log(Si/Ca) fall, and Ca, Sr, log (Ca/Ti) and log(Ca/Fe) increase. Ti and Fe fall slightly initially, though remain relatively high, then rise again in the second half of the unit. Wispy vertical lines in X-radiographs indicate bioturbation. Radiocarbon dates the base of this unit to 11,567–12,101 cal BP (2σ).

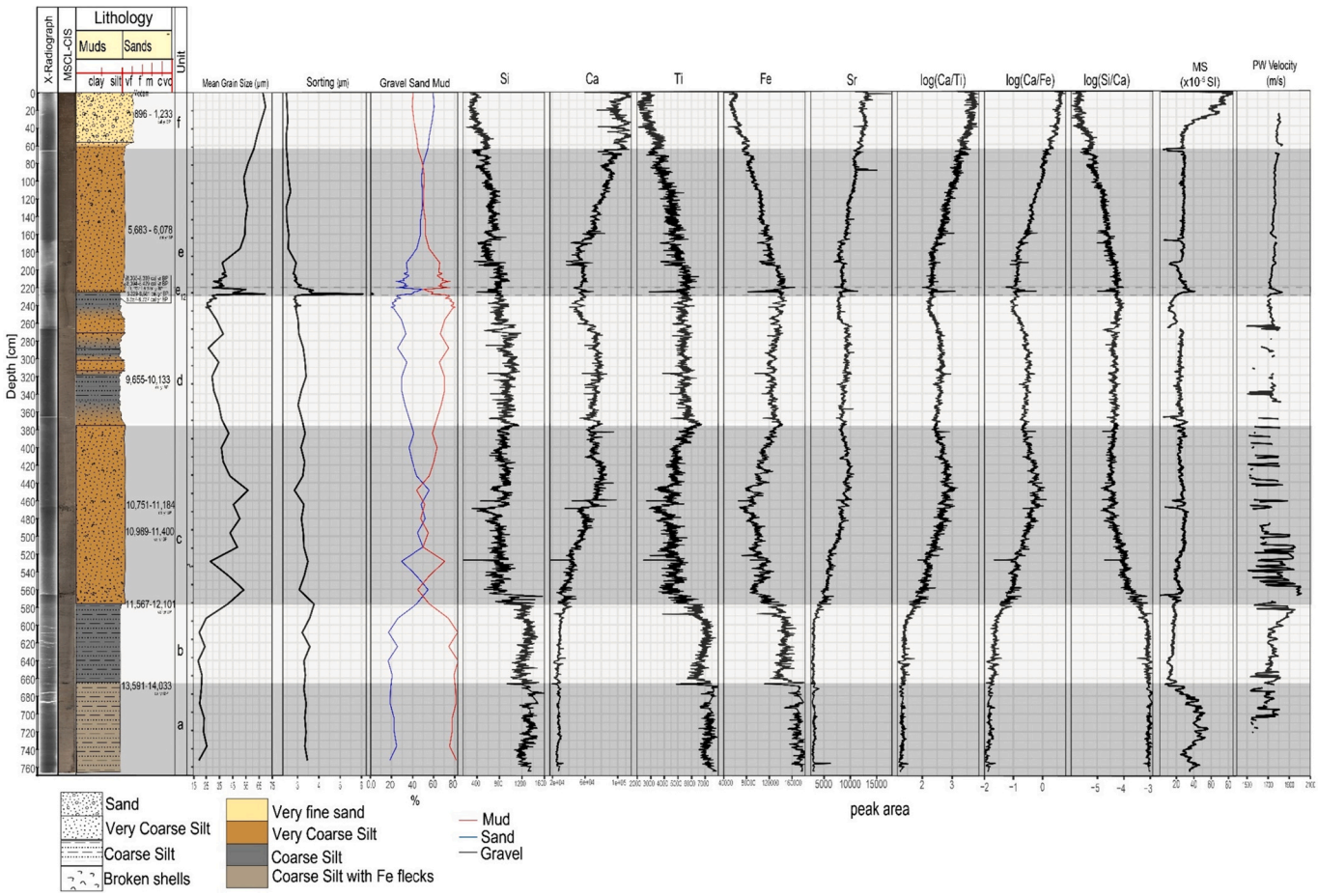

Fig. 4. PC012 full core physical properties data (X-Radiograph, MSCL-CIS, core log, Mean Grain Size, Sorting Capacity, XRF elemental data, Magnetic susceptibility (MS) and P-wave Velocity). Exact depths of calibrated age range 95% (2σ) (cal yr BP) can be seen in Table 1.

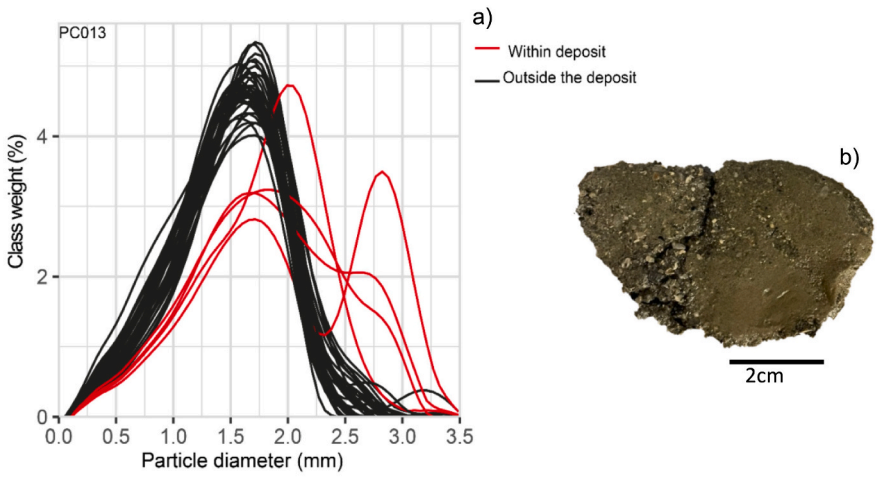

Fig. 5. a) Grain size distribution plot for PC013. Red lines represent depths within the deposit (260-264 cm). Black lines represent the distributions for all depths surrounding the layer (243-260 cm, 264-284 cm). b) Sediment from PC013 263-364 cm showing mixture of large and small grains, and black gravels. (For interpretation of the references to colour in this figure legend, the reader is referred to the web version of this article.)

4.2.4. Unit D

The base of Unit D is at 375 cm and marks the transition into a unit which is mainly olive grey, poorly sorted coarse silt, with some very coarse silt. From the cleaned core surface it is challenging to determine the transitions between the coarse silt and very coarse silt, but X-radiographs reveal regions of finely laminated silts which are graded into coarser sediments. Wispy vertical lines in X-radiographs indicate bioturbation. Small shell fragments are sparsely distributed throughout. Grain sizes are mainly unimodal, in particular from 272 cm to the top of the unit. Elemental data show little fluctuation throughout this section, and magnetic susceptibility remains between 20×10^{-5} and 30×10^{-5} SI. The modelled median age for the base of this unit is 10,159 cal BP.

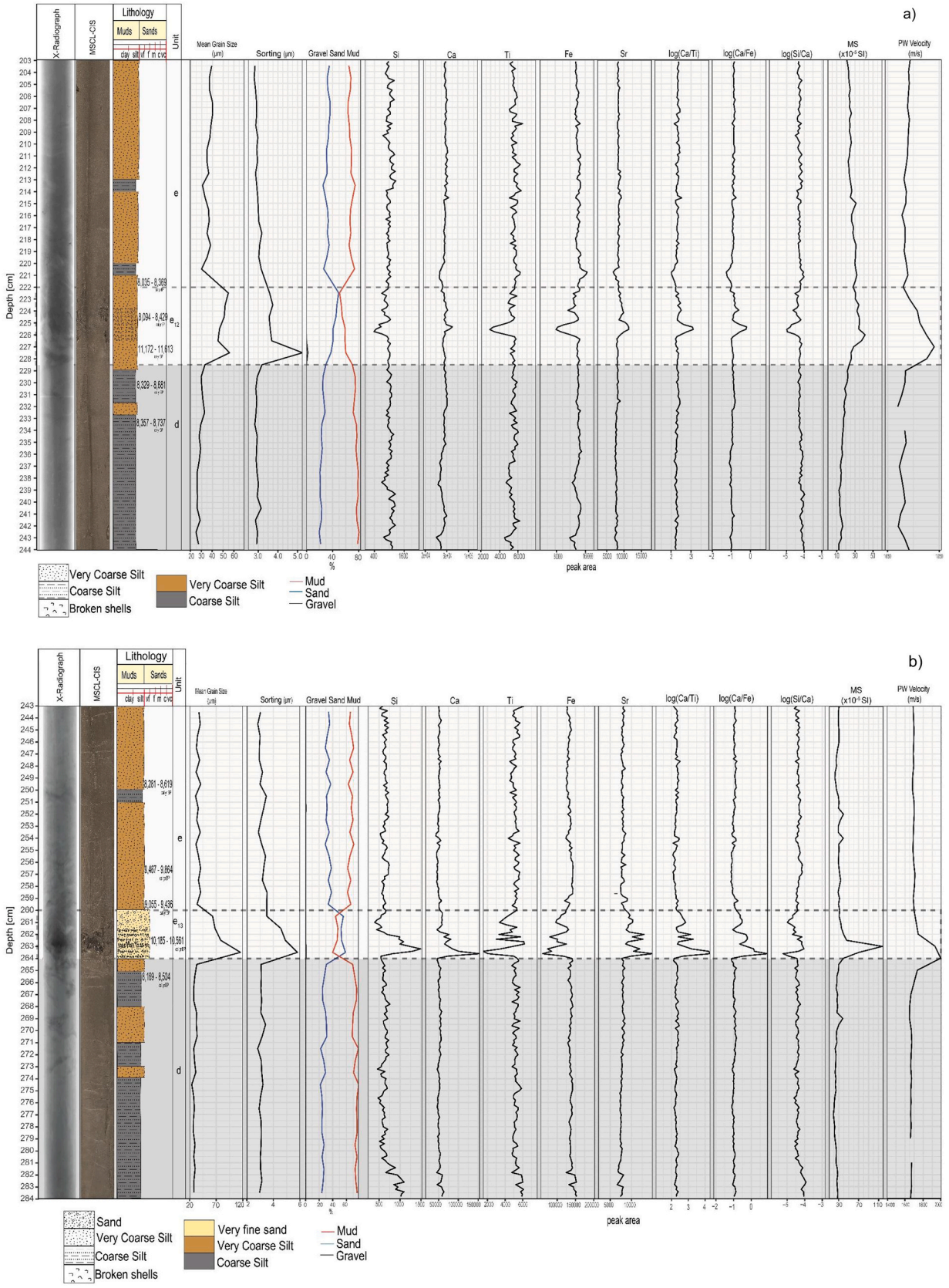

Fig. 6. Event deposit in (a) PC012, sub-unit e12 (b) PC013, sub-unit e13. X-Radiograph, MSCL-CIS, core log, Mean Grain Size, Sorting Capacity XRF elemental data, Magnetic suscptibility (MS) and P Wave Velociy (PW Vel). Exact depths of calibrated age range 95% (2σ) (cal yr BP) can be seen in Table 1.

4.2.5. Unit E

The base of Unit E in PC012 is defined by a distinct facies between 228 and 222 cm, named sub-unit e12 (Fig. 6a). It is this sub-unit that was visually identified and hypothesised to occur as a result of a North Sea tsunami. At 228 cm, there is an increase in grain size to very coarse silt, the presence of the gravel fraction for the first time within the core, and a reduction in sorting capacity. Although lower than the preceding sediment, the mud content within e12 is still relatively high (40–60%). Between 225 and 226 cm, there is a small but defined peak in Sr, log(Ca/Ti), log(Ca/Fe) and MS, and small drop in Fe, Ti, Si and log(Si/Ca). From 227 to 228 sediments are bimodally distributed, and 222-225 cm bi/tri-modally distributed. In the middle of bed e12 (227-225 cm) sediments are unimodally distributed. Shell fragments and coarse grains, some black in colour (Fig. 6), can be seen visually in the split core from 227 to 222 cm (Fig. 6a). X-radiographs indicate a change in sedimentology during this bed, but a clear base and top to unit is hard to define, likely due to bioturbation (Fig. 7).

From 220 cm to the top of Unit E (65 cm), sediments return to a unimodal distribution. There is a slight transition in colour from olive-grey to olive upward throughout the unit. The mean grain size increases to the top, and shell fragments become more common near the top. XRF shows increasing Ca, Sr, log(Ca/Ti), log(Ca/Fe) and decreasing Fe, Ti, Si, log(Si/Ca). Active bioturbation traces in the X-radiographs are somewhat reduced in comparison to Units D and C.

In core PC013, there is a unit showing similar but more pronounced changes in sediment properties from 264 to 260 cm, named sub-unit e13 (Fig. 6b). This sub-unit begins with a sudden increase in mean grain size at 263-264 cm (115 μm) to fine sand, a change in grain size distribution from unimodal to bi, tri and polymodal from 264 to 261 cm and reduction in sorting capacity. The increase in coarse grain size can be seen visually and abruptly at the core surface at 264 cm, and within the X-radiograph (Fig. 7). A concentration of shell fragments and black

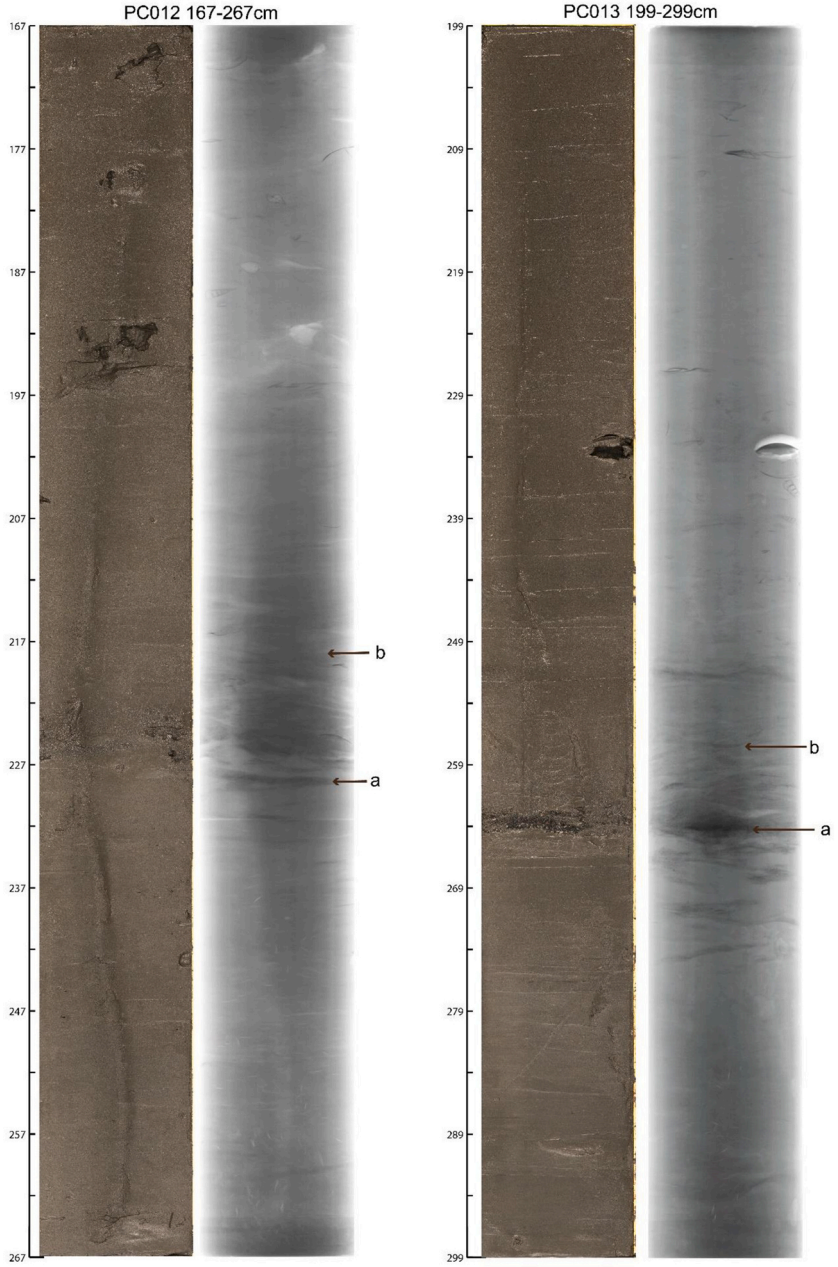

Fig. 7. MSCL-CIS and X-radiographs of core sections containing event deposits e12 and e13. (a) may represent an erosive base. (b) may represent reworked coarse material deposited by submarine debris flow or turbidity current.

grains is also visible at this depth. Grain size fines upwards throughout the section back to coarse silt. A clear peak in MS and PW velocity can be seen at 263 cm. XRF data show a peak in Ca, Sr, log(Ca/Ti), log(Ca/Fe) and a fall in Fe, Ti, Si, log(Si/Ca) 262–263.5. Above this sub-unit, sediments are unimodally distributed very coarse silts, largely similar to PC012.

4.2.6. Unit F

The base of Unit F is at 65 cm and is defined by a transition to olive coloured poorly sorted fine sand containing whole bivalves and shell fragments. Sediments are unimodally distributed, and show high Ca, log (Ca/Ti), log(Ca/Fe) and Sr values, alongside low Si, TI and log(Si/Ca). At the top of this section, MS values rise rapidly. The modelled median age for the base of this unit is 2499 cal BP.

4.3. Sub-bottom profiler

The depth conversion used allowed identified sedimentary units to be matched with the sub-bottom profiler data at the core location (Fig. 8). At the base of the profile, below the depth of the core, there is a soft and diffuse reflector with acoustic penetration beneath. Above the reflector, but below Unit A, distinct laminations are present.

The basal depths of Units A-D do not show distinct acoustic responses. There is a distinct reflector within Unit C ~ 4.8 m below the core surface. The sea floor reflection and the base of Unit F match the very strong reflections at the top of the sub-bottom profile. Although not prominent, a faint reflection is visible corresponding to e12 and e13 in the sub-bottom profile. This faint reflector can be tracked laterally over longer distances in the full sub-bottom profile (Fig. 8c).

5. Discussion

5.1. Interpretation of sedimentary units and event deposits

The sub-bottom profile data allow for some suggestions to be made about the sediments beyond the maximum core depth. The morphology and hydroacoustic characteristics of the soft and diffuse reflector near the base of the sub-bottom profile suggests it may represent a buried moraine landform. Above this reflector, but below Unit A, distinct laminations are present, which may represent glaci-proximal sediments. It is important to note that additional sedimentological evidence is required to confirm these hypotheses.

5.1.1. Unit A

Unit A displays textural laminations (visible in X-radiographs), high MS and Fe values, and higher sedimentation rates. We suggest this unit represents a low energy distal glacimarine sequence with tidewater glaciers, or a period seasonal sea ice cover; the massive laminations may be the result of sediment plumes from tidewater glaciers, or anoxic conditions when sea ice prevails (Graham et al., 2010). This unit shows similarity with Unit L3 described in glaci-distal North Sea sediments by Graham et al. (2010). Bradwell et al. (2019) suggest that the final deglaciation of Shetland was around 16.5 ± 0.3–14.9 ± 2.0 ka, and tidewater glaciers had retreated beyond the marine limit by ~16 ka, which favours the latter sea-ice interpretation. X-radiographs do not suggest the unit contains large ice-rafted detritus (IRD) drop stones, which are associated with glaci-marine sediments (Bradwell et al., 2019; Graham et al., 2010), again suggesting sea-ice is a more feasible interpretation. The present suite of analyses cannot confirm the presence or absence of finer IRD, although high MS values are commonly associated with glaci-marine sediments and IRD on the European margin due to the input of terrigenous ferromagnetic material (Peters et al., 2008; Scourse et al., 2009). Further analysis of sediments using IRD flux quantification techniques could be used to strengthen the interpretation of this unit.

5.1.2. Unit B

Unit B may be considered a low energy, a fully marine postglacial sequence. Reduced MS and lack of laminations in this unit may be consistent with the absence of tidewater glaciers or seasonal sea ice, leading to increased oxygenation of bottom water and more active bioturbation. The reduction in magnetic susceptibility may be the result of dilution by increased organic matter input, or a reduction in minerogenic input from heavy mineral rich metamorphic rocks. Radiocarbon dates at the base and top of this unit (13,591–14,033 cal BP to 11,567–12,101 cal BP (2σ)) constrain it to the late deglacial. Thus, high sedimentation rates may be explained by a lack of established land-

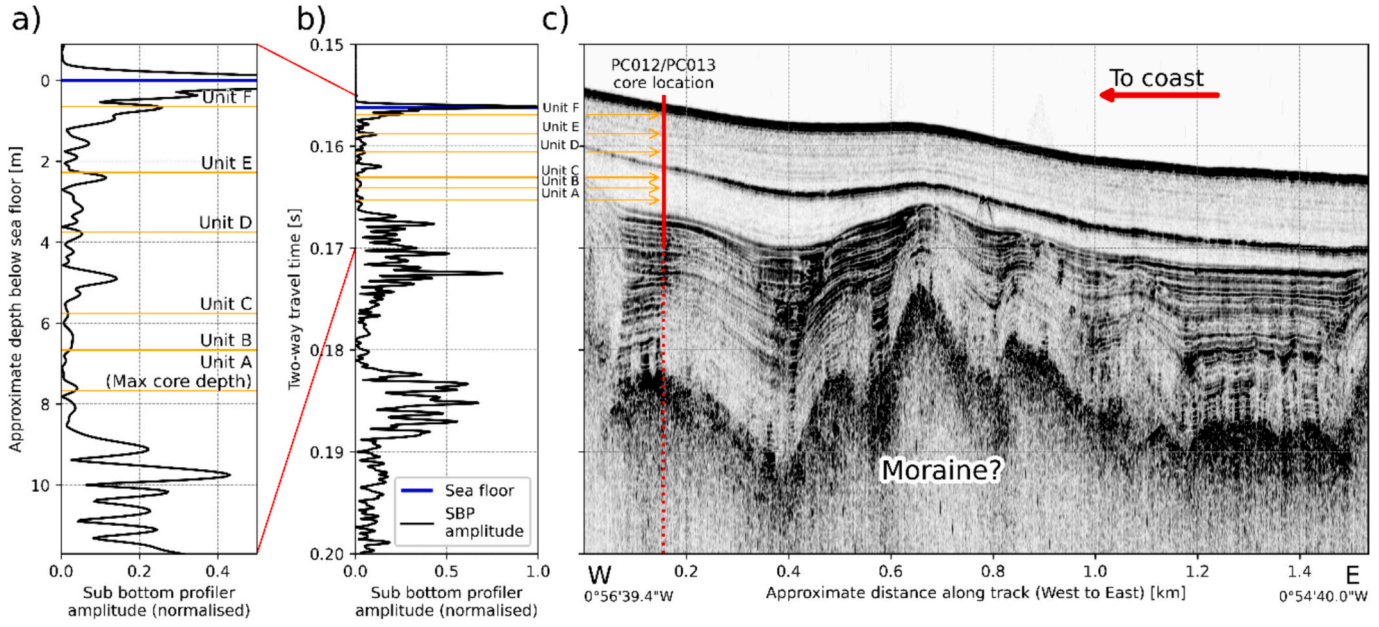

Fig. 8. Sub-bottom profiler data matched with Units A-F based on cores PC012 and PC013. a) vertical echogram at the core location of PC012/PC013. TWT is converted to approximate depth below sea floor using filtered P-wave velocity from core logging data. Note that while the acoustic responses for the base of Unit F is very strong, the responses for others are less strong, but still visible; b) vertical echogram at the core location of PC012/PC013; c) Sub-bottom profiler data over distance covering the wider FB A sampling area. Note that even weaker signals, like the base of Unit E, can be traced along the whole profile.

stabilising vegetation in para-glacial settings, which leads to increased erosion and subsequently high deposition, especially in inshore depocenters (Ballantyne, 2002) such as the Fetlar Basin. In addition, lower sea levels during this period (Fig. 2a) would increase the proximity of the core site to land, and as such result in higher sedimentation rates.

5.1.3. Unit C

Unit C is interpreted to represent a shallow (RSL 12 ka ~51 m, Fig. 2a) but fully marine environment. The radiocarbon date of 11,567–12,101 cal BP (2σ) at the base of the unit suggests this sedimentary change represents the start of the Holocene. The increase in Ca, Sr and log(Ca/Ti) throughout this unit is concurrent with the increase in visible shell material, and may represent an increase in productivity as the basin becomes fully marine. Palaeo-sea surface temperature records suggest an early Holocene Climate Optimum in the North Atlantic, 12,000–10,000 cal yr BP (Hald et al., 2007). These warmer temperatures may have contributed to increased productivity. The very coarse poorly sorted silts may indicate more active tidal currents; during periods of higher tidal current activity finer grained materials remain in suspension and transported, whereas coarser material remains on the seabed (Soulsby, 1997).

The distinct reflector within Unit C ~ 4.8 m below the core surface corresponds to a median modelled age of 11,171 cal BP, and may represent a gas front (Naudts et al., 2009), or a section of whole intact small bivalve shells. The occurrence of a bow-tie effect on this reflector, an artifact of the acoustic data acquisition (Yilmaz, 1987), points to the presence of a large obstacle with a high reflectivity. Due to a depth of >4 m, below the burial depth of sea cables in the area, this is likely a large clast or boulder, or small pockmark.

5.1.4. Unit D

Age models indicate that Unit D represents the early Holocene. Elemental ratios indicate a more stable environment, perhaps due to increasing water depths (Fig. 2a). The general fining of sediment and lower sedimentation rate in this unit could be indicative of reduced terrigenous input as vegetation established onshore (Nørgaard-Pedersen et al., 2006). This suggestion is supported by pollen analyses, which propose a transition from herbaceous vegetation to woodland in Shetland around 9.7 ka BP (Bennett et al., 1992; Hulme and Shirriffs, 1994), thus stabilising terrestrial sediments. Laminations of finer grained sediment may indicate quiescent or low energy conditions with no or limited bioturbation, as suggested by low bed stress vectors. Coarser laminations may represent sudden inputs of increased terrestrial or riverine input, which is likely in this coastal setting.

5.1.5. Unit E

The sub-units at the base of Unit E are discussed in a subsequent section. Radiocarbon dates suggest this unit contains mid- to late Holocene sediments. The coarsening upward of mean grain size within this unit align rising modelled bed stress vectors (Fig. 2b) during the mid-late Holocene. The presence of shell fragments and rising log(Ca/Ti) and Sr values suggest that the Fetlar Basin became increasingly productive throughout this period.

5.1.6. Unit F

Elemental data in Unit F may represent a stabilisation of the marine environment in the late Holocene. The high Ca, log(Ca/Ti), log(Ca/Fe) and Sr values levels indicate high marine productivity. This unit displays the coarsest grain size within the entire sequence, and closely follows trends in modelled bed stress vectors, with highest values occurring after 3 ka (Fig. 2b). The coarsening of sediments may also indicate an increase in tidal amplitude as relative sea level attained its peak in the late Holocene.

5.1.7. Event deposits – Sub-units e12 and e13

Sub-units e12 and e13 show contrasting characteristics to the surrounding early Holocene sediments, indicating a possible abrupt change in hydrodynamic conditions. ^{14}C dating of the sub-units provides evidence that these coarse lenses are coeval with the Storegga event (8180–8080 cal yr BP (Bondevik et al. (2012), updated to IntCal20 by Rush et al. (2023)). In addition to the timing of this deposit, evidence of onshore deposits (Bondevik et al., 2003; Dawson et al., 1988; Dawson and Smith, 2000), wave heights (A. Dawson et al., 2020; Hill et al., 2023; Woodroffe et al., 2023) and offshore flow velocities (Bondevik et al., 2024) of the Storegga tsunami on Shetland and Northern Scotland, leads us to propose that this event generated the deposit observed in this study. This proposal is supported further by the physical and geochemical characteristics of sub-units e12 and e13.

Analysis of grain size profiles can be used to support interpretations of tsunami deposits, with characteristics including increases in mean grain size (Costa et al., 2021; Feist et al., 2023; Smedile et al., 2020), upward fining of sediments (Feist et al., 2023; Ikehara et al., 2021a, 2021b; Yhasnara et al., 2023), and reductions in sorting capacity (Feist et al., 2023; Feldens et al., 2012).

In this study, both e12 and e13 display a clear and sharp increase in mean grain size identifiable in visual logging and PSA, as well as the presence of gravel for the first time within the profile. This increase in grain size and presence of gravel suggests a degree of transport of coarser allochthonous material to the core site, in addition to possible local suspended sediment. Modelling suggests that on the shallow shelf around Shetland, maximum flow velocities caused by the Storegga tsunami may have reached up to 5 m/s, which is well over the 1 m/s velocity required to move grain sizes from 5 μm to 7 mm (fine silt to fine pebbles) (Bondevik et al., 2024). As such, these velocities have the capability to transport large grains from outcrops or shallower settings to the core site. Additionally, such flow velocities would be capable of creating the sharp basal erosional contact seen particularly in e13, which are observed in other offshore tsunami deposits (e.g. Feist et al., 2023; Feldens et al., 2012; Smedile et al., 2020). The gradual fining of sediment through sub-unit e13 (Fig. 6), is generated as finer particles settle from the suspension cloud on top of the coarse grains when currents have reduced (Costa et al., 2021).

Sub-units e12 and e13 also show a reduction in sorting capacity. In particular, poor sorting capacity has been noted as a characteristic of tsunami deposits resulting from debris flows (Feist et al., 2023), due to the low sorting capacity of this process (Shanmugam, 1997). Additionally, the high mud content within the deposits leads us to propose generation of e12 and e13 by submarine debris flow; muddy sediments increase the plasticity of debris flows, and differentiate them from turbidity currents (Lowe, 1976).

Increased concentrations of shell material are also common in offshore tsunami deposits and suggested to result from either resuspension and settling of local seabed material, or backwash of shallower calcareous material (Costa et al., 2021; Quintela et al., 2016; Smedile et al., 2020; Yhasnara et al., 2023). This can be seen in both e12 and e13, although to a greater extent in e13, and is supported by XRF data via peaks in log(Ca/Te) and Sr, which are commonly associated with increased calcareous material (Chagué-Goff et al., 2017). In the Fetlar Basin deposits, high concentrations of shell material in comparison with the preceding and overlying sediments may point towards the material within the deposit being derived from a shallower marine setting with higher shell content.

Anomalous radiocarbon dates within tsunami deposits have been noted by Feist et al. (2023). In the Fetlar Basin, the anomalous radiocarbon ages within the event deposits suggest a degree of backwash induced material transport. This is because the radiocarbon ages from the underlying early Holocene sediments in PC012 are in ascending chronostratigraphic order (Fig. 3), suggesting they are in situ. Therefore, older carbonate which generated the anomalous radiocarbon dates within the deposit must have been transported laterally from the inner shelf to the core site. In the Fetlar Basin, nearshore steep slopes likely saw reduced sedimentation rates during the early Holocene. This means

that less material needs to be eroded by tsunami or debris flows to access Late glacial and early Holocene sediments in these areas. It is therefore hypothesised that these basin slopes are the source regions for allochthonous material. In addition to this allochthonous material, it is possible that some material within the deposit is re-suspended autochthonous material, as there is a small hiatus between the date base of the event deposit in PC013 and the early Holocene sediments. This suggests that some sediments in the Fetlar Basin were eroded by the incoming tsunami wave, or the base of a submarine debris flow.

Increases in magnetic susceptibility (MS) noted here may also support the interpretation of the sub-units as tsunami deposits, as increases in MS can indicate high concentrations of terrestrial material in marine sediments. In this context, it could suggest the erosion and transport of terrestrial material by the tsunami wave and backwash. Peaks in MS can be seen within both deposits, and in e13 this corresponds with a peak in terrigenous/clay associated elements. In contrast, in PC012 there is a relative reduction in the magnetic elements (e.g. Fe, Ti), but it is possible that the high concentration of Ca diluted the signal of terrestrial sediments within the deposit, and therefore there may still be terrigenous material present. This has been observed in modelling studies, in which a greater proportion of offshore deposit sediment is of marine rather than of terrestrial origin (Yoshii et al., 2017). Detailed analysis of the minerology and provenance of lithic grains within the offshore deposit is beyond the scope of this study, but preliminary analysis indicates the presence of angular granite fragments and angular mica and hornblende. The angularity of these fragments indicates that it is eroded material that has not been present in the marine environment for a long period, or was closer to its original source, and thus eroded by the tsunami. The presence of hornblende aligns with the work of Cascalho et al. (2016) who studied the heavy mineral assemblage of onshore Storegga deposits on Shetland and suggested that hornblende (derived from the Moine Formation on the mainland of Shetland) may have been transported offshore by backwash, as it showed the lowest concentration in onshore deposits. The concentration of these lithic grains may have caused the increase in MS at this level. Additional analyses of the minerogenic content of the deposit may reveal further evidence of terrestrial material, and reveal the origin of the tsunami backwash. However, in coastal locations such as the Fetlar basin, terrestrial material is likely commonly washed onto the shallow shelf, so may not provide direct evidence of terrestrial inundation.

Gaffney et al. (2020) suggest peaks and troughs in deposit elemental data may represent multiple backwash flows. The XRF data for deposit e13 show two cycles between 264 and 261 cm, which oscillate between an increase in shell indicative elements (Sr, log(Ca/Ti)) and terrigenous/clay associated elements (Fe, Si). However, visual inspection of the deposit and grain sorting data alongside XRF data indicate that the variability is most likely a function of the highly variable and poorly sorted mix of lithic grains and shell fragments rather than multiple distinct shell layers. The single massive deposit may also be explained by the nature of landslide generated tsunami, which often generate unidirectional waves, and exert the majority of energy in the initial wave, followed by smaller lower energy waves. Thus, it may be that the initial wave was the only one powerful enough to generate backwash deposits at this distance offshore (Cascalho et al., 2016).

Hydroacoustic surveys using sub-bottom profilers can be useful for identifying offshore tsunami deposits; reflectors in sub-bottom profiles have been associated with changes in sediment type, correlated to palaeo-tsunami events (Feist et al., 2023; Goodman-Tchernov and Austin, 2015). It may be expected that the sharp material change at the base of Unit E would produce a similar reflection to that of the seabed, due to the similar shelly coarse-grained nature of the sediment. However, the low thickness of event deposits e12 and e13 likely attenuates the resulting amplitude due to tuning effects (Avseth et al., 2005). Similarly, on the Algarve shelf, tsunami deposits have been identified in sediment cores where the hydroacoustic surveys showed weak or indistinct reflectors (Feist et al., 2023). Amongst the cores collected in Feist et al., (2023)), the sequences which showed the least distinct reflectors were the furthest offshore and had the weakest geochemical and geophysical signals. This may suggest that sheltered locations around Shetland closer to the coast may contain thicker deposits detectable in hydroacoustic surveys related to the Storegga tsunami.

5.2. e12 and e13 - Depositional process

Previous investigation into offshore deposits has included both recent tsunami, predominantly the 2011 Japanese Tōhoku tsunami (Ikehara et al., 2021a, 2021b; Irizuki et al., 2019; Tamura et al., 2015) and the 2004 Indian Ocean tsunami (Feldens et al., 2009; Sakuna et al., 2012; Veerasingam et al., 2014), and palaeo-tsunamis, primarily on the Algarve shelf (Portugal) (Feist et al., 2023; Quintela et al., 2016; Veerasingam et al., 2014; Yhasnara et al., 2023) and in Augusta Bay (Eastern Sicily) (Smedile et al., 2020; Smedile et al., 2011). These studies have been key in developing a toolkit for palaeo-tsunami identification, and the findings have recently been summarised by Costa et al. (2021). Despite relatively well-developed criteria for identification, there has been a call for further descriptions of offshore deposits, in particular their geochemical signatures (Shinozaki, 2021). This is because site specific factors such as local bathymetry and sediment supply influence the depositional process, meaning a general characterization of offshore deposits is difficult to establish (Costa et al., 2021).

Based on the radiocarbon ages, increase in grain size, poor sorting of sediments, the erosive base, abundance of shell material and associated elemental data, and high mud content above, e12 and e13 are interpreted as debris flow deposits coeval with the Storegga tsunami. The following depositional process, as visualised in Fig. 9, is proposed:

During the incoming tsunami phase, currents are generated which induce some erosion of bottom sediments and contribute to sharp erosional base noted in deposits (Fig. 9b). The subsequent tsunami backwash initiates a submarine debris flow on the shallow shelf. As the debris flow travels downslope, erosion occurs at the base. This erosion, particularly on the steep slopes, entrains and ingests Late-glacial and early Holocene marine sediments and shell material (Fig. 9c). The debris flow may also contain terrestrial material, if backwash from the tsunami land inundation phase reaches this distance offshore. As tsunami currents subside, particles dispersed within the turbid water column begin to settle on top of the debris flow to form a graded fining upward sequence (Fig. 9d). After the event, all debris flow and suspended material settles. In locations where bioturbation and mixing is less prevalent, a graded sequence develops (e.g. PC013). Post-depositional alteration can cause mixing that obscures a distinguishable graded sequence (Fig. 9e). This depositional process is similar to that described by Feist et al. (2023) and Riou et al. (2020). In contrast to on the Algarve shelf (Feist et al., 2023), the high mud content in the Fetlar Basin represents a singular debris rather than grain flow followed by debris flow. These interpretations may be used to guide assessments of offshore deposits in similar deep sheltered basins with steep slopes.

In some cases, tsunami deposits containing allochthonous material are interpreted to result from turbidity currents (Ikehara et al., 2021b; Ikehara et al., 2014; Seike et al., 2017). However, in the Fetlar Basin, poor sorting and the absence of a graded bed indicated deposition by debris flow rather than turbidity current (Shanmugam, 1997). In addition, tsunami deposits interpreted as turbidites display some characteristics of the classical Bouma (Bouma, 1962) and Lowe (Lowe, 1982) sequences, including massive well sorted graded sediment (Ta, S3), laminations (Tb, S1) and ripples (Tc) (Ikehara et al., 2021b, Ikehara et al., 2014; Seike et al., 2017). The X-radiographs in this study may reveal evidence of bioturbated laminations, which could relate to stage Tb of the Bouma sequence, as in Seike et al. (2017). However, there is a degree of ambiguity in X-radiographs (Fig. 7), as the features may rather represent coarse material from a debris flow which was reworked by subsequent currents, or bioturbated. The suggestion of post-depositional reworking of the deposit is supported by the anomalous radiocarbon

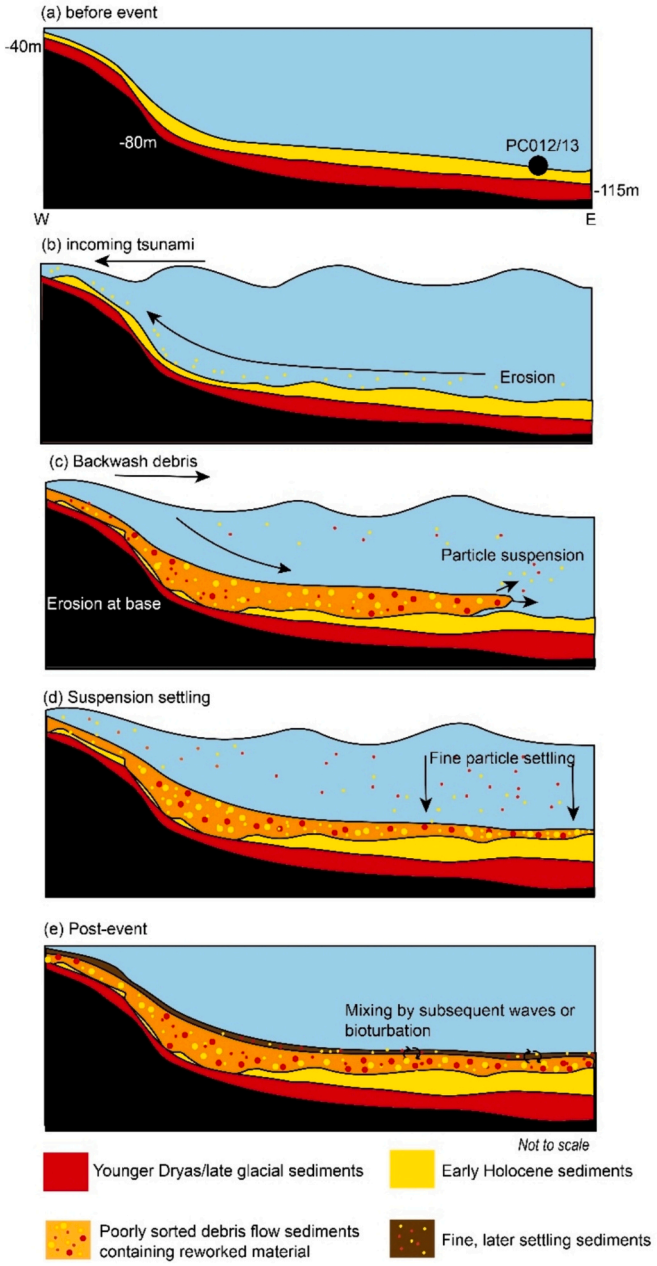

Fig. 9. Depositional process for sub-units e12 and e13. PC012 and PC013 are located near the bottom of the Fetlar Basin. The basin geomorphology can be seen in Fig. 1; steep slopes are present, in particular on the western side. (a) Pre-8.2 ka event. (b) incoming tsunami creates currents which induce some erosion of bottom sediments and cause sharp erosional base. (c) Debris flow is initiated on the shallow shelf. As it travels downslope, erosion occurs at the base of the debris flow, and early Holocene as well as younger dryas sediments are picked up. This may contain terrestrial material. (d) Debris flow deposit settles. Fine particles dispersed within the water column begin to settle on top of debris flow as tsunami currents subside in a graded fining upward sequence. (e) Debris flow and fine material settle. In locations where bioturbation and mixing is less prevalent, the graded sequence develops (e.g. PC013). Post deposition alteration can cause mixing and removes distinguishable graded sequence.

date of 8281–8619 cal yr BP (2σ), approximately 10 cm above the top of the deposit in PC013. This explanation seems the most plausible, as the grain size, sorting and XRF data resume background Holocene characteristics at this depth.

5.3. Other possible trigger mechanisms

The Storegga slide, which subsequently lead to the Storegga tsunami, is proposed to have been triggered by increased pore pressure and reduction in soil strength of sediments deposited in previous interglacials (contourites) (Bryn et al., 2005). Earthquake activity, rapid loading of glacial sediments, and gas hydrate melting are the suggested causes of increased pressure, but a combination of these likely contributed to the slip (Bryn et al., 2005). The proposal of an earthquake-induced slip in the lower slide complex is supported by suggestions of earthquakes greater than magnitude 7 in northern Norway. These were caused by post-glacial glacio-isostatic rebound of the Scandinavian region (Bryn et al., 2005; Bungum et al., 2005; Kvalstad et al., 2005). In the Storegga area specifically, crustal faults created during the Late Jurassic–Early Cretaceous period may have been reactivated by pressure caused by sediment loading in the North Sea Fan, generating an earthquake (Bryn et al., 2005). Suggestions of an earthquake in the region thus raises the possibility that e12 and e13 are a result of a tremor-induced submarine debris flow. However, there is currently no estimation for the magnitude of earthquake required to trigger the Storegga slide, or an estimation of the seismic hazard zone. This is likely due to the fact it is challenging to quantify the contribution of each trigger mechanism to the slide, and as such make an estimation of the earthquake magnitude.

Tsunami deposits can sometimes be challenging to discern from high energy storm deposits, as they can display similar characteristics such as increased grain size. It is therefore important to determine the storm wave base depth at the time of deposition (Costa et al., 2021). For a wave to entrain sediments (wave base), the depth of the water must be equal to or less than approximately half of the wavelength (Peters and Loss, 2012). Based on our calculation of a palaeo-water depth of ~88 m at the core site, a storm with a minimum wavelength of 176 m would be required to generate a wave base that would mobilise sediments. A recent rogue wave event has been identified in the mid-North Sea with a wavelength of 500 m (Pleskachevsky et al., 2012), but lack of data on modern or palaeo-storm wavelengths in the Fetlar Basin makes it challenging to establish if a separate powerful storm generated the deposit observed in this study as opposed to the Storegga tsunami wave. Additionally, the Fetlar Basin is situated on the East of Shetland in a loaction relatively sheltered from North Atlantic swells which dominate the wave climate in the region (Cox, 2021). The sediments prior to and after the deposit in both cores also do not show signals of regular storminess, and offshore storm deposits also tend to display better sorting of sediments than observed in the present study (Costa et al., 2021). Combined with the radiocarbon age coincidence with the Storegga Tsunami, these data indicate the deposit is a result of the Storegga event rather than another coincidental storm.

5.4. Other Holocene tsunami

Despite the preservation of the Storegga event in these sediment sequences, it was not possible to detect a signal of the Garth tsunami at ~5500 cal BP or the Dury Voe tsunami ~1500 cal BP. During the later Holocene, background sediments have a generally coarser grain size and higher Ca content, which may have resulted in the deposits caused by the later tsunami being indistinguishable from the background sediment using the current suite of proxies. Additionally, active bioturbation and increased bed stress during the later Holocene (Fig. 2b) may have disturbed the deposits, again making them indistinguishable from the background sediments. Alternatively, it may be that the smaller magnitude of these events meant backwash currents capable of creating deposits at this distance offshore were not generated. Sedimentary signals of the recently proposed Nyegga Slide tsunami (Karstens et al., 2023) are likely undetectable in this setting as the Fetlar Basin was glaciated until at least 17 ka BP (Bradwell et al., 2019). Investigation in other basins, or locations within the Fetlar Basin may reveal signals of

the Garth and Dury Voe tsunami in the offshore domain, due to the variability in spatial preservation of signals. In addition, other coring locations may present thicker deposits, allowing further investigation into the hydrodynamic conditions, and potential multiple wave regime, of all three Holocene tsunami.

5.5. Implications for the 8.2 ka event in marine sedimentary sequences

The evidence presented here for reworking of sediments and allochthonous material transport has relevance for the identification of the coeval 8.2 ka cold event in marine sedimentary sequences. Similar results have been found by Bondevik et al. (2024), who identify reworking and allochthonous material within a tsunami-generated turbidity deposit in a marine sequence from the Vøring plateau at 1048 m water depth, 200 km off the Norwegian coast. This deposit is 2 cm thick, displays an erosive boundary layer followed by an upward fining of sediment, and was originally thought to be a deposit resulting from the 8.2 ka cold event. However, radiocarbon dating of foraminifera within the layer to ~11 ka, $\delta^{18}O$ values consistent with the Younger Dryas or Early Holocene, and allochthonous shallow water foraminifera indicated that this layer was a result of reworking and transportation of older shallow material by Storegga tsunami turbidity currents. The evidence presented here and in Bondevik et al. (2024) highlight the significant re-working around 8.2 ka and thus the potential to misinterpret the palaeoclimatic sequence in both shallow and deep waters. Further coring around Shetland and in the North Sea would be useful for determining the extent of the submarine debris flow identified in this study, and to map out the seafloor regions, and thus paleoclimate records impacted by the Storegga event.

5.6. Implications for hazard risk assessment around Shetland

Prior to this study, research into marine Storegga tsunami deposits was limited to three distinct settings; a shallow location (6 m palaeowater depth) that was below sea level (SL) during the Storegga event but is now above SL due to isostatic uplift (Bondevik et al., 1997); an area that was above SL during the event but is now submerged due to eustatic sea level rise (Gaffney et al., 2020; Walker et al., 2020); the continental slope (~1000 m water depth) that has remained fully submerged since the tsunami (Bondevik et al., 2024). Whilst these studies are useful for understanding the tsunami dynamics, data from marine sediment cores can improve our assessment of the impact of tsunami on the subtidal shelf, where much infrastructure in the North Sea is located.

This study has interpreted a submarine debris flow within the Fetlar Basin resulting from the Storegga event. This has relevance for present and future seabed infrastructure, such as the extant oil and gas pipelines in the Fetlar Basin, as submarine debris flows and turbidity currents can have major impacts on seafloor structures (Bruschi et al., 2006; Chen et al., 2022; Qian et al., 2023; White et al., 2016). Whilst assessing the scale of the potential submarine debris flow offshore Shetland is beyond the scope of this study, future research should focus on mapping the extent of the Storegga event deposits offshore, and assess the vulnerability of seabed infrastructure.

Offshore sediment sequences have the potential to provide evidence of tsunami which are undetected onshore due to anthropogenic disturbance or weathering of sediments (Costa et al., 2021). This study does not find evidence of tsunami later in the Holocene, thus does not imply risk assessments should be revised in terms of increased event frequency. There is, however, the possibility that such events may be identified at other locations offshore Shetland. Further work in other basins and water depths should be completed to rule out the identification of further Holocene tsunami and to develop hazard risk assessments in terms of event frequency.

6. Conclusion

We present a detailed description of deglacial and Holocene sediments in the Fetlar Basin, offshore east Shetland. Within the sedimentary sequence, we provide the first published evidence for the offshore signal of the Storegga event around Shetland, a location where there is significant onshore evidence for the tsunami. Two core sequences from the basin show distinguishable lenses with increases in grain size, a reduction in sorting capacity, increased shell concentrations and peaks in associated elements (log(Ca/Fe), log(Ca/Ti) and Sr). These signatures, alongside evidence of sediment reworking based on radiocarbon dating and high mud content, suggest this layer was deposited from tsunami-driven backwash debris flow. The high concentration of carbonates within the section suggests backwash material of mainly marine origin, although peaks in magnetic susceptibility and the presence of coarse grains may indicate some material of terrestrial origin. Further work on the mineralogy and total organic carbon of the layer may provide evidence that the deposit contains terrestrial material. Differences in the physical properties of the event layers within the two cores show evidence of lateral variation in tsunami signatures, even over small spatial scales.

^{14}C dating provides clear evidence of sediment reworking. This highlights the need for caution in researching the coincident 8.2 ka cooling event in marine sediments in wave-affected areas due to potential confusion of cold signal indicators with reworked material from underlying cold stage deposits. No evidence for later Holocene tsunami was detected in these sedimentary sequences, perhaps due to increased disturbance from tidal currents or bioturbation.

Future research should focus on mapping the extent of offshore deposits to produce a more complete insight into tsunami hydrodynamics in this region, and potentially identify signals of other palaeo tsunami. This study highlights the potential for tsunami to impact the deep subtidal seabed via tsunami induced debris flows, and therefore to impact hydrocarbon infrastructure around Shetland and across the North Sea. Further work should be completed to assess the risk and likelihood of damage to this infrastructure should a similar event occur in future.

Acknowledgement and Funding

This project has received funding from the University of Exeter, and the European Research Council (ERC) under the European Union's Horizon 2020 research and innovation programme (grant agreement No 85648). We thank the British Ocean Sediment Core Research Facility (BOSCORF) for supporting the generation and analyses of XRF core scanning, X-radiography, MSCL-S, MSCL-XYZ and MSCL-CIS data used in this study. The generation of these data was funded by the 5-day bursary scheme for PhD students and Early Career Researchers at BOSCORF. Thanks is also given to lab staff at the Scottish Universities Environmental Research Centre NEIF Environmental Radiocarbon Laboratory (SUERC), East Kilbride, and Dr. Xiaomei Xu at the Keck Carbon Cycle AMS Facility, University of California, Irvine, USA for analysing radiocarbon samples. Finally, we thank the crew and shipboard party of the RRS Discovery DY150 research cruise for facilitating and aiding sediment core recovery.

Credit authorship contribution statement

Jane L. Earland: Writing – review & editing, Writing – original draft, Visualization, Project administration, Methodology, Investigation, Formal analysis, Data curation, Conceptualization. **James D. Scourse:** Writing – review & editing, Supervision, Investigation, Funding acquisition, Conceptualization. **Tobias Ehmen:** Writing – original draft, Formal analysis, Data curation. **Sev Kender:** Writing – review & editing, Supervision. **Philippa Ascough:** Writing – review & editing, Data curation.

Declaration of competing interest

The authors declare no competing financial or personal relationship interests.

Data availability

The manuscript and appendices contain all available data. Additional information regarding cruise DY150 can be found in the cruise report (Scourse et al., 2022).

Appendix A. ITRAX, MSCL-CIS, MSCL-S, MSCL-XYZ and ScoutXcan set-up

Scanner	Resolution/set-up	Data
Geotek MSCL-CIS (Core Imaging System)	N/A	High resolution images
A Geotek MSCL-S (Standard), fitted with a P-wave velocity sensor, gamma ray density meter and a non contact resistivity sensor	2 cm Count time: 10 s	P-Wave Amplitude, P-Wave Velocity, Gamma density
Geotek MSCL-XYZ was fitted with a Bartington magnetic susceptibility point sensor and a Konica Minolta spectrophotometer	0.5 cm resolution Count time: 5 s	Magnetic susceptibility, greyscale reflectance, and CIELAB colour (L*, a*, b*)
Geotek ScoutXcan X-Ray Imaging Scanner	Resolution: 84 μm per pixel Voltage: 123 kV Current: 455 mA Cu filter: 1.0 mm	High resolution x-radiographs
Itrax X-ray Fluorescence (XRF) COX Analytical Systems	Resolution:2 mm Voltage: 55 kV Current: 0 mA Exposure time: 15 s	Elemental properties

References

Alley, R.B., Ágústsdóttir, A.M., 2005. The 8k event: cause and consequences of a major Holocene abrupt climate change. Quat. Sci. Rev. 24, 1123–1149. https://doi.org/10.1016/j.quascirev.2004.12.004.

Ascough, P.L., Cook, G.T., Dugmore, A.J., Scott, E.M., Freeman, S.P.H.T., 2005. Influence of Mollusk Species on Marine ΔR Determinations. Radiocarbon 47, 433–440. https://doi.org/10.1017/S0033822200035219.

Ascough, P., Bompard, N., Garnett, M.H., Gulliver, P., Murray, C., Newton, J.-A., Taylor, C., 2024. 14C measurement of samples for environmental science applications at the National Environmental Isotope Facility (NEIF) Radiocarbon Laboratory, SUERC, UK. Radiocarbon 1–12. https://doi.org/10.1017/rdc.2024.9. Published online.

Austin, W.E.N., Telford, R.J., Ninnemann, U.S., Brown, L., Wilson, L.J., Small, D.P., Bryant, C.L., 2011. North Atlantic reservoir ages linked to high Younger Dryas atmospheric radiocarbon concentrations. In: Global and Planetary Change, Rapid Climate Change: Lessons from the Recent Geological Past, 79, pp. 226–233. https://doi.org/10.1016/j.gloplacha.2011.06.011.

Avseth, P., Mukerji, T., Mavko, G., 2005. Quantitative Seismic Interpretation: applying Rock Physics Tools to Reduce Interpretation Risk. Cambridge University Press, Cambridge. https://doi.org/10.1017/CBO9780511600074.

Ballantyne, C.K., 2002. Paraglacial geomorphology. Quat. Sci. Rev. 21, 1935–2017. https://doi.org/10.1016/S0277-3791(02)00005-7.

Bennett, K.D., Boreham, S., Sharp, M.J., Switsur, V.R., 1992. Holocene history of environment, vegetation and human settlement on Catta Ness, Lunnasting, Shetland. J. Ecol. 80, 241. https://doi.org/10.2307/2261010.

Bishop, T., 2022. itraxR: Itrax Data Analysis Tools.

Blaauw, M., Christen, J.A., 2011. Flexible paleoclimate age-depth models using an autoregressive gamma process. Bayesian Anal. 6, 457–474. https://doi.org/10.1214/11-BA618.

Blott, S.J., Pye, K., 2001. GRADISTAT: a grain size distribution and statistics package for the analysis of unconsolidated sediments. Earth Surf. Process. Landf. 26, 1237–1248. https://doi.org/10.1002/esp.261.

Bondevik, S., 2019. Tsunami from the Storegga landslide. In: Encyclopedia of Complexity and Systems Science, 153–185. https://doi.org/10.1007/978-3-642-27737-5_644-1.

Bondevik, S., Svendsen, J.I., Mangerud, J., 1997. Tsunami sedimentary facies deposited by the Storegga tsunami in shallow marine basins and coastal lakes, western Norway. Sedimentology 44, 1115–1131. https://doi.org/10.1046/j.1365-3091.1997.d01-63.x.

Bondevik, S., Mangerud, J., Dawson, S., Dawson, A., Lohne, Ø., 2003. Record-breaking height for 8000-year-old tsunami in the North Atlantic. Eos 84. https://doi.org/10.1029/2003EO310001.

Bondevik, S., Mangerud, J., Dawson, S., Dawson, A., Lohne, Ø., 2005. Evidence for three North Sea tsunamis at the Shetland Islands between 8000 and 1500 years ago. Quat. Sci. Rev. 24, 1757–1775. https://doi.org/10.1016/j.quascirev.2004.10.018.

Bondevik, S., Stormo, S.K., Skjerdal, G., 2012. Green mosses date the Storegga tsunami to the chilliest decades of the 8.2 ka cold event. Quat. Sci. Rev. 45, 1–6. https://doi.org/10.1016/j.quascirev.2012.04.020.

Bondevik, S., Risebrobakken, B., Gibbons, S.J., Rasmussen, T.L., Løvholt, F., 2024. Contamination of 8.2 ka cold climate records by the Storegga tsunami in the Nordic Seas. Nat. Commun. 15, 2904. https://doi.org/10.1038/s41467-024-47347-9.

Bouma, A.H., 1962. Sedimentology of some Flysch Deposits: A Graphic Approach to Facies Interpretation. Elsevier Pub. Co., Amsterdam.

Bradley, S.L., Milne, G.A., Shennan, I., Edwards, R., 2011. An improved glacial isostatic adjustment model for the British Isles. J. Quat. Sci. 26, 541–552. https://doi.org/10.1002/jqs.1481.

Bradwell, T., Small, D., Fabel, D., Clark, C.D., Chiverrell, R.C., Saher, M.H., Dove, D., Callard, S.L., Burke, M.J., Moreton, S.G., Medialdea, A., Bateman, M.D., Roberts, D. H., Golledge, N.R., Finlayson, A., Morgan, S., Cofaigh, C., 2019. Pattern, style and timing of British–Irish Ice Sheet retreat: Shetland and northern North Sea sector. J. Quat. Sci. 36, 681–722. https://doi.org/10.1002/jqs.3163.

Bristow, C., Buck, L., 2021. GPR survey of storegga tsunami deposits, shetland islands UK, and geohazard discussion. In: Presented at the Engineering and Mining Geophysics 2021. European Association of Geoscientists & Engineers, pp. 1–8. https://doi.org/10.3997/2214-4609.202152184.

Bruschi, R., Bughi, S., Spinazzé, M., Torselletti, E., Vitali, L., 2006. Impact of debris flows and turbidity currents on seafloor structures. Nor. Geol. Tidsskr. 86, 317–336.

Bryn, P., Berg, K., Forsberg, C.F., Solheim, A., Kvalstad, T.J., 2005. Explaining the Storegga Slide. Mar. Pet. Geol. 22, 11–19. https://doi.org/10.1016/j.marpetgeo.2004.12.003.

Bungum, H., Lindholm, C., Faleide, J.I., 2005. Postglacial seismicity offshore mid-Norway with emphasis on spatio-temporal–magnitudal variations. In: Marine and Petroleum Geology, Ormen Lange - an integrated study for the safe development of a deep-water gas field within the Storegga Slide Complex, NE Atlantic continental margin, 22, pp. 137–148. https://doi.org/10.1016/j.marpetgeo.2004.10.007.

Cappelli, E.L.G., Austin, W.E.N., 2020. Marine bivalve feeding strategies and radiocarbon ages in Northeast Atlantic Coastal Waters. Radiocarbon 62, 107–125. https://doi.org/10.1017/RDC.2019.68.

Cascalho, J., Costa, P., Dawson, S., Milne, F., Rocha, A., 2016. Heavy mineral assemblages of the Storegga tsunami deposit. Sediment. Geol. 334, 21–33. https://doi.org/10.1016/j.sedgeo.2016.01.007.

Chagué-Goff, C., Szczuciński, W., Shinozaki, T., 2017. Applications of geochemistry in tsunami research: a review. Earth Sci. Rev. 165, 203–244. https://doi.org/10.1016/j.earscirev.2016.12.003.

Chen, Y., Zhang, L., Wei, X., Xu, J., Fu, S., Liao, C., 2022. Debris-flow-induced damage assessment for a submarine pipeline network in regional-scale natural terrain. Eng. Geol. 311, 106917 https://doi.org/10.1016/j.enggeo.2022.106917.

Costa, P., Andrade, C., 2020. Tsunami deposits: present knowledge and future challenges. Sedimentology 67, 1189–1206. https://doi.org/10.1111/sed.12724.

Costa, P., Feist, L., Dawson, A., Stewart, I., Reicherter, K., Andrade, C., 2021. Chapter 11 - an overview on offshore tsunami deposits. In: Shiki, T., Tsuji, Y., Yamazaki, T., Nanayama, F. (Eds.), Tsunamiites, Second edition. Elsevier, pp. 183–192. https://doi.org/10.1016/B978-0-12-823939-1.00011-2.

Cox, A., 2021. Shetland Isles Scottish Marine Regions Assessment 2020 (SMR2020). Marine Scotland. Scottish Government.

Dawson, A.G., Shi, S., 2000. Tsunami deposits. Pure Appl. Geophys. 157, 875–897. https://doi.org/10.1007/s000240050010.

Dawson, S., Smith, D.E., 2000. The sedimentology of Middle Holocene tsunami facies in northern Sutherland, Scotland, UK. Mar. Geol. 170, 69–79. https://doi.org/10.1016/S0025-3227(00)00066-9.

Dawson, A., Long, D., Smith, D.E., 1988. The Storegga slides: evidence from eastern Scotland for a possible tsunami. Mar. Geol. 82, 271–276. https://doi.org/10.1016/0025-3227(88)90146-6.

Dawson, A., Dawson, S., Bondevik, S., 2006. A late Holocene Tsunami at Basta Voe, Yell, Shetland Isles. Scott. Geogr. J. 122, 100–108. https://doi.org/10.1080/00369220600917404.

Dawson, A.G., Dawson, S., Bondevik, S., Costa, P.J.M., Hill, J., Stewart, I., 2020. Reconciling Storegga tsunami sedimentation patterns with modelled wave heights: a discussion from the Shetland Isles field laboratory. Sedimentology 67, 1344–1353. https://doi.org/10.1111/sed.12643.

De Martini, P.M., Bruins, H.J., Feist, L., Goodman-Tchernov, B.N., Hadler, H., Lario, J., Mastronuzzi, G., Obrocki, L., Pantosti, D., Paris, R., Reicherter, K., Smedile, A., Vött, A., 2021. The Mediterranean Sea and the Gulf of Cadiz as a natural laboratory for paleotsunami research: recent advancements. Earth Sci. Rev. 216, 103578 https://doi.org/10.1016/j.earscirev.2021.103578.

Engel, M., Schön, I., Patel, T., Pawłowski, J., Szczuciński, W., Dawson, S., Garrett, E., Heyvaert, V.M.A., 2020. Chapter 20 - paleogenetic approaches in tsunami deposit studies. In: Engel, M., Pilarczyk, J., May, S.M., Brill, D., Garrett, E. (Eds.), Geological Records of Tsunamis and Other Extreme Waves. Elsevier, pp. 427–442. https://doi.org/10.1016/B978-0-12-815686-5.00020-1.

Engel, M., Hess, K., Dawson, S., Patel, T., Koutsodendris, A., Vakhrameeva, P., Klemt, E., Kempf, P., Schön, I., Heyvaert, V.M.A., 2023. Sedimentary evidence of the late Holocene tsunami in the Shetland Islands (UK) at Loch Flugarth, northern Mainland. Boreas. https://doi.org/10.1111/bor.12635.

Estrella-Martínez, J., Ascough, P.L., Schöne, B.R., Scourse, J.D., Butler, P.G., 2019. 8.2 ka event North Sea hydrography determined by bivalve shell stable isotope geochemistry. Sci. Rep. 9, 6753. https://doi.org/10.1038/s41598-019-43219-1.

Evelpidou, N., Karkani, A., Polidorou, M., Saitis, G., Zerefos, C., Synolakis, C., Repapis, C., Tzouxanioti, M., Gogou, M., 2022. Palaeo-Tsunami events on the Coasts of Cyprus. Geosciences 12, 58. https://doi.org/10.3390/geosciences12020058.

Feist, L., Costa, P., Bellanova, P., Bosnic, I., Santisteban, J.I., Andrade, C., Brückner, H., Duarte, J.F., Kuhlmann, J., Schwarzbauer, J., Vött, A., Reicherter, K., 2023. Holocene offshore tsunami archive – tsunami deposits on the Algarve shelf (Portugal). Sediment. Geol. 448, 106369 https://doi.org/10.1016/j.sedgeo.2023.106369.

Feldens, P., Schwarzer, K., Szczuciński, W., Stattegger, K., Sakuna, D., Somgpongchaiykul, P., 2009. Impact of 2004 tsunami on seafloor morphology and offshore sediments, Pakarang Cape, Thailand. Pol. J. Environ. Stud. 18.

Feldens, P., Schwarzer, K., Sakuna, D., Szczuciński, W., Sompongchaiyakul, P., 2012. Sediment distribution on the inner continental shelf off Khao Lak (Thailand) after the 2004 Indian Ocean tsunami. Earth Planet Sp 64, 7. https://doi.org/10.5047/eps.2011.09.001.

Folk, R.L., Ward, W.C., 1957. Brazos River bar [Texas]; a study in the significance of grain size parameters. J. Sediment. Res. 27, 3–26. https://doi.org/10.1306/74D70646-2B21-11D7-8648000102C1865D.

Gaffney, V., Fitch, S., Bates, M., Ware, R.L., Kinnaird, T., Gearey, B., Hill, T., Telford, R., Batt, C., Stern, B., Whittaker, J., Davies, S., Sharada, M.B., Everett, R., Cribdon, R., Kistler, L., Harris, S., Kearney, K., Walker, J., Muru, M., Hamilton, D., Law, M., Finlay, A., Bates, R., Allaby, R.G., 2020. Multi-proxy characterisation of the storegga tsunami and its impact on the early holocene landscapes of the Southern North Sea. Geosciences 10, 270. https://doi.org/10.3390/geosciences10070270.

Garrett, E., Pilarczyk, J.E., Brill, D., 2018. Preface to marine geology special issue: geological records of extreme wave events. Mar. Geol. Rec. Extreme Wave Events 396, 1–5. https://doi.org/10.1016/j.margeo.2017.11.006.

Goff, J., Chagué, C., Nichol, S., Jaffe, B., Dominey-Howes, D., 2012. Progress in palaeotsunami research. Sediment. Geol. 243–244, 70–88. https://doi.org/10.1016/j.sedgeo.2011.11.002.

Goodman-Tchernov, B.N., Austin, J.A., 2015. Deterioration of Israel's Caesarea Maritima's ancient harbor linked to repeated tsunami events identified in geophysical mapping of offshore stratigraphy. J. Archaeol. Sci. Rep. 3, 444–454. https://doi.org/10.1016/j.jasrep.2015.06.032.

Graham, A.G.C., Lonergan, L., Stoker, M.S., 2010. Depositional environments and chronology of late Weichselian glaciation and deglaciation in the central North Sea. Boreas 39, 471–491. https://doi.org/10.1111/j.1502-3885.2010.00144.x.

Grauert, M., Björck, S., Bondevik, S., 2001. Storegga tsunami deposits in a coastal lake on Suouroy, the Faroe Islands. Boreas 30, 263–271. https://doi.org/10.1111/j.1502-3885.2001.tb01045.x.

Hald, M., Andersson, C., Ebbesen, H., Jansen, E., Klitgaard-Kristensen, D., Risebrobakken, B., Salomonsen, G.R., Sarnthein, M., Sejrup, H.P., Telford, R.J., 2007. Variations in temperature and extent of Atlantic Water in the northern North Atlantic during the Holocene. Quat. Sci. Rev. 26, 3423–3440. https://doi.org/10.1016/j.quascirev.2007.10.005.

Hamilton, E.L., 1971. Prediction of in-situ acoustic and elastic properties of marine sediments. Geophysics 36, 266–284. https://doi.org/10.1190/1.1440168.

Heaton, T.J., Köhler, P., Butzin, M., Bard, E., Reimer, R.W., Austin, W.E.N., Ramsey, C.B., Grootes, P.M., Hughen, K.A., Kromer, B., Reimer, P.J., Adkins, J., Burke, A., Cook, M. S., Olsen, J., Skinner, L.C., 2020. Marine20—the marine radiocarbon age calibration curve (0–55,000 cal BP). Radiocarbon 62, 779–820. https://doi.org/10.1017/RDC.2020.68.

Heier-Nielsen, S., Conradsen, K., Heinemeier, J., Knudsen, K.L., Nielsen, H.L., Rud, N., Sveinbjörnsdóttir, Á.E., 1995. Radiocarbon dating of shells and foraminifera from the skagen core, denmark: evidence of reworking. Radiocarbon 37, 119–130. https://doi.org/10.1017/S0033822200030551.

Hess, K., Engel, M., Patel, T., Vakhrameeva, P., Koutsodendris, A., Klemt, E., Hansteen, T. H., Kempf, P., Dawson, S., Schön, I., Heyvaert, V.M.A., 2023. A 1500-years record of North Atlantic storminess from the Shetland Islands (UK) (preprint). In Review. https://doi.org/10.21203/rs.3.rs-2731397/v1.

Hill, J., Rush, G., Peakall, J., Johnson, M., Hodson, L., Barlow, N.L.M., Bowman, E.T., Gehrels, W.R., Hodgson, D.M., Kesserwani, G., 2023. Resolving tsunami wave dynamics: Integrating sedimentology and numerical modelling. Depositional Rec. 9, 1046–1065. https://doi.org/10.1002/dep2.247.

Hulme, P.D., Shirriffs, J., 1994. The Late-glacial and Holocene vegetation of the Lang Lochs Mire area, Gulberwick, Shetland: a pollen and macrofossil investigation. New Phytol. 128, 793–806. https://doi.org/10.1111/j.1469-8137.1994.tb04040.x.

Ikehara, K., Irino, T., Usami, K., Jenkins, R., Omura, A., Ashi, J., 2014. Possible submarine tsunami deposits on the outer shelf of Sendai Bay, Japan resulting from the 2011 earthquake and tsunami off the Pacific coast of Tohoku. In: Marine Geology, In the wake of the 2011 Tohoku-oki tsunami - three years on 358, pp. 120–127. https://doi.org/10.1016/j.margeo.2014.11.004.

Ikehara, K., Irino, T., Saito, Y., 2021a. The 2011 Tohoku-oki tsunami-induced sediment remobilization on the Sendai shelf, Japan, from a comparison of pre- and post-tsunami surface sediments. Sci. Rep. 11, 7864. https://doi.org/10.1038/s41598-021-87152-8.

Ikehara, K., Usami, K., Irino, T., Omura, A., Jenkins, R.G., Ashi, J., 2021b. Characteristics and distribution of the event deposits induced by the 2011 Tohoku-oki earthquake and tsunami offshore of Sanriku and Sendai, Japan. Sediment. Geol. 411, 105791 https://doi.org/10.1016/j.sedgeo.2020.105791.

Irizuki, T., Fujiwara, O., Yoshioka, K., Suzuki, A., Tanaka, Y., Nagao, M., Kawagata, S., Kawano, S., Nishimura, O., 2019. Geochemical and micropaleontological impacts caused by the 2011 Tohoku-oki tsunami in Matsushima Bay, northeastern Japan. Mar. Geol. 407, 261–274. https://doi.org/10.1016/j.margeo.2018.10.007.

Karstens, J., Haflidason, H., Berndt, C., Crutchley, G.J., 2023. Revised Storegga Slide reconstruction reveals two major submarine landslides 12,000 years apart. Commun Earth Environ 4, 1–9. https://doi.org/10.1038/s43247-023-00710-y.

Klitgaard-Kristensen, D., Sejrup, H.P., Haflidason, H., Johnsen, S., Spurk, M., 1998. A regional 8200 cal. Yr BP cooling event in Northwest Europe, induced by final stages of the Laurentide ice-sheet deglaciation? J. Quat. Sci. 13, 165–169. https://doi.org/10.1002/(SICI)1099-1417(199803/04)13:2<165::AID-JQS365>3.0.CO;2-#.

Kvalstad, T.J., Andresen, L., Forsberg, C.F., Berg, K., Bryn, P., Wangen, M., 2005. The Storegga slide: evaluation of triggering sources and slide mechanics. In: Marine and Petroleum Geology, Ormen Lange - an integrated study for the safe development of a deep-water gas field within the Storegga Slide Complex, NE Atlantic continental margin, 22, pp. 245–256. https://doi.org/10.1016/j.marpetgeo.2004.10.019.

Lowe, D.R., 1976. Grain flow and grain flow deposits. J. Sediment. Res. 46, 188–199. https://doi.org/10.1306/212F6EF1-2B24-11D7-8648000102C1865D.

Lowe, D.R., 1982. Sediment gravity flows; II, Depositional models with special reference to the deposits of high-density turbidity currents. J. Sediment. Res. 52, 279–297. https://doi.org/10.1306/212F7F31-2B24-11D7-8648000102C1865D.

Malvern Panalytical, 2024. Mastersizer 3000 User Manual. URL. https://www.malvernpanalytical.com/en/support/product-support/mastersizer-range/mastersizer-3000#manuals.

Marine Scotland, 2019. Oil and Gas - Hydrocarbon Pipelines (NSTA and OceanWise).

Naudts, L., De Batist, M., Greinert, J., Artemov, Y., 2009. Geo- and hydro-acoustic manifestations of shallow gas and gas seeps in the Dnepr paleodelta, northwestern Black Sea. Lead. Edge 28, 1030–1040. https://doi.org/10.1190/1.3236372.

Nørgaard-Pedersen, N., Austin, W.E.N., Howe, J.A., Shimmield, T., 2006. The Holocene record of Loch Etive, western Scotland: influence of catchment and relative sea level changes. Mar. Geol. 228, 55–71. https://doi.org/10.1016/j.margeo.2006.01.001.

Nott, J., 2003. The importance of prehistoric data and variability of hazard regimes in natural hazard risk assessment – examples from Australia. Nat. Hazards 30, 43–58. https://doi.org/10.1023/A:1025072929280.

Peters, S.E., Loss, D.P., 2012. Storm and fair-weather wave base: a relevant distinction? Geology 40, 511–514. https://doi.org/10.1130/G32791.1.

Peters, C., Walden, J., Austin, W.E.N., 2008. Magnetic signature of European margin sediments: Provenance of ice-rafted debris and the climatic response of the British ice sheet during Marine Isotope Stages 2 and 3. J. Geophys. Res. Earth 113. https://doi.org/10.1029/2007JF000836.

Pleskachevsky, A.L., Lehner, S., Rosenthal, W., 2012. Storm observations by remote sensing and influences of gustiness on ocean waves and on generation of rogue waves. Ocean Dyn. 62, 1335–1351. https://doi.org/10.1007/s10236-012-0567-z.

Qian, X., Liu, Z., Xu, J., 2023. New insights into quantifying the stable impact forces of a submarine debris flow on a pipeline. Ocean Eng. 274, 114060 https://doi.org/10.1016/j.oceaneng.2023.114060.

Quintela, M., Costa, P., Fatela, F., Drago, T., Hoska, N., Andrade, C., Freitas, M.C., 2016. The AD 1755 tsunami deposits onshore and offshore of Algarve (South Portugal): Sediment transport interpretations based on the study of Foraminifera assemblages. In: Quaternary International, QuicklakeH Special Issue: Rapidly Changing Large Lakes and Human Response, 408, pp. 123–138. https://doi.org/10.1016/j.quaint.2015.12.029.

Rasmussen, H., Bondevik, S., Corner, G.D., 2018. Holocene relative sea level history and Storegga tsunami run-up in Lyngen, northern Norway. J. Quat. Sci. 33, 393–408. https://doi.org/10.1002/jqs.3021.

Reimer, P.J., Reimer, R.W., 2001. A marine reservoir correction database and on-line interface. Radiocarbon 43, 461–463. https://doi.org/10.1017/S0033822200038339.

Riou, B., Chaumillon, E., Chagué, C., Sabatier, P., Schneider, J.-L., Walsh, J.-P., Zawadzki, A., Fierro, D., 2020. Backwash sediment record of the 2009 South Pacific Tsunami and 1960 Great Chilean Earthquake Tsunami. Sci. Rep. 10, 4149. https://doi.org/10.1038/s41598-020-60746-4.

Rohling, E.J., Pälike, H., 2005. Centennial-scale climate cooling with a sudden cold event around 8,200 years ago. Nature 434, 975–979. https://doi.org/10.1038/nature03421.

Romundset, A., Bondevik, S., 2011. Propagation of the Storegga tsunami into ice-free lakes along the southern shores of the Barents Sea. J. Quat. Sci. 26, 457–462. https://doi.org/10.1002/jqs.1511.

Rush, G., Garrett, E., Bateman, M.D., Bigg, G.R., Hibbert, F.D., Smith, D.E., Gehrels, W. R., 2023. The magnitude and source of meltwater forcing of the 8.2 ka climate event constrained by relative sea-level data from eastern Scotland. Quaternary Science Advances 12, 100119. https://doi.org/10.1016/j.qsa.2023.100119.

Russell, N., Cook, G.T., Ascough, P.L., Scott, E.M., 2015. A period of calm in Scottish seas: a comprehensive study of ΔR values for the northern British Isles coast and the consequent implications for archaeology and oceanography. Quat. Geochronol. 30, 34–41. https://doi.org/10.1016/j.quageo.2015.08.001.

Sakuna, D., Szczuciński, W., Feldens, P., Schwarzer, K., Khokiattiwong, S., 2012. Sedimentary deposits left by the 2004 Indian Ocean tsunami on the inner continental shelf offshore of Khao Lak, Andaman Sea (Thailand). Earth Planet Sp 64, 931–943. https://doi.org/10.5047/eps.2011.08.010.

Scourse, J.D., Haapaniemi, A.I., Colmenero-Hidalgo, E., Peck, V.L., Hall, I.R., Austin, W. E.N., Knutz, P.C., Zahn, R., 2009. Growth, dynamics and deglaciation of the last British–Irish ice sheet: the deep-sea ice-rafted detritus record. Quat. Sci. Rev. 28, 3066–3084. https://doi.org/10.1016/j.quascirev.2009.08.009.

Scourse, J.D., Afrifa, K., Byrne, L., Crowley, D., Earland, J., Ehmen, T., Frøslev, T., Greenall, C., Harland, J., Heard, Z., Höche, N., Holman, L., Huang, Q., Langkjær, E., Mason, M., Nelson, E., Nemeth, Z., Reynolds, D., Robson, H., Roman Gonzalez, A., Scherer, P., Scolding, J., Short, J., Wilkin, J., Wilson, D., 2022. RRS Discovery DY150 Cruise Summary Report.

Scourse, J., Ward, S., Wainwright, A., Bradley, S., Wilson, J.K., Guo, J., 2024. An interactive visualization and data portal tool (PALTIDE) for relative sea level and palaeotidal simulations of the northwest European shelf seas since the last Glacial Maximum. J. Quaternary Sci. https://doi.org/10.1002/jqs.3615.

Seike, K., Kobayashi, G., Kogure, K., 2017. Post-depositional alteration of shallow-marine tsunami-induced sand layers: a comparison of recent and ancient tsunami deposits, Onagawa Bay, northeastern Japan. Island Arc 26, e12174. https://doi.org/10.1111/iar.12174.

Shanmugam, G., 1997. The Bouma Sequence and the turbidite mind set. Earth Sci. Rev. 42, 201–229. https://doi.org/10.1016/S0012-8252(97)81858-2.

Shinozaki, T., 2021. Geochemical approaches in tsunami research: current knowledge and challenges. Geosci. Lett. 8, 6. https://doi.org/10.1186/s40562-021-00177-9.

Smedile, A., De Martini, P.M., Pantosti, D., Bellucci, L., Del Carlo, P., Gasperini, L., Pirrotta, C., Polonia, A., Boschi, E., 2011. Possible tsunami signatures from an integrated study in the Augusta Bay offshore (Eastern Sicily—Italy). Mar. Geol. 281, 1–13. https://doi.org/10.1016/j.margeo.2011.01.002.

Smedile, A., Molisso, F., Chagué, C., Iorio, M., De Martini, P.M., Pinzi, S., Collins, P.E.F., Sagnotti, L., Pantosti, D., 2020. New coring study in Augusta Bay expands understanding of offshore tsunami deposits (Eastern Sicily, Italy). Sedimentology 67, 1553–1576. https://doi.org/10.1111/sed.12581.

Soulsby, R., 1997. Dynamics of Marine Sands.

Stuiver, M., Reimer, P.J., 1993. CALIB rev. 8. Radiocarbon 35, 215–230.

Switzer, A.D., Yu, F., Gouramanis, C., Soria, J.L.A., Pham, D.T., 2014. Integrating different records to assess coastal hazards at multi-century timescales. coas 70, 723–729. https://doi.org/10.2112/SI70-122.1.

Tamura, T., Sawai, Y., Ikehara, K., Nakashima, R., Hara, J., Kanai, Y., 2015. Shallow-marine deposits associated with the 2011 Tohoku-oki tsunami in Sendai Bay, Japan. J. Quat. Sci. 30, 293–297. https://doi.org/10.1002/jqs.2786.

Taylor, J., Selby, D., Lloyd, J.M., Podrecca, L., Masterson, A.L., Sageman, B.B., Szidat, S., 2024. Palaeoenvironmental reconstruction of Loch Duart (NW Scotland, UK) since the last Glacial Maximum: implications from a multiproxy approach. J. Quat. Sci. 39, 6–23. https://doi.org/10.1002/jqs.3566.

Udden, J.A., 1914. Mechanical composition of clastic sediments. GSA Bull. 25, 655–744. https://doi.org/10.1130/GSAB-25-655.

Veerasingam, S., Venkatachalapathy, R., Basavaiah, N., Ramkumar, T., Venkatramanan, S., Deenadayalan, K., 2014. Identification and characterization of tsunami deposits off southeast coast of India from the 2004 Indian Ocean tsunami: Rock magnetic and geochemical approach. J Earth Syst Sci 123, 905–921. https://doi.org/10.1007/s12040-014-0427-y.

Wagner, B., Bennike, O., Klug, M., Cremer, H., 2007. First indication of Storegga tsunami deposits from East Greenland. J. Quat. Sci. 22, 321–325. https://doi.org/10.1002/jqs.1064.

Walker, J., Gaffney, V., Fitch, S., Muru, M., Fraser, A., Bates, M., Bates, R., 2020. A great wave: the Storegga tsunami and the end of Doggerland? Antiquity 94, 1409–1425. https://doi.org/10.15184/aqy.2020.49.

Ward, S.L., Neill, S.P., Scourse, J.D., Bradley, S.L., Uehara, K., 2016. Sensitivity of palaeotidal models of the northwest European shelf seas to glacial isostatic adjustment since the last Glacial Maximum. Quat. Sci. Rev. 151, 198–211. https://doi.org/10.1016/j.quascirev.2016.08.034.

Webster, J.M., Yokoyama, Y., Cotterill, C., Expedition 325 Scientists, 2011. Methods. In: Proceedings of the Integrated Ocean Drilling Program. https://doi.org/10.2204/iodp.proc.325.102.2011.

Wentworth, C.K., 1922. A scale of grade and class terms for clastic sediments. J. Geol. 30, 377–392. https://doi.org/10.1086/622910.

White, D.J., Randolph, M.F., Gaudin, C., Boylan, N.P., Wang, D., Boukpeti, N., Zhu, H., Sahdi, F., 2016. The impact of submarine slides on pipelines: outcomes from the COFS-MERIWA JIP. In: Presented at the Offshore Technology Conference, OnePetro. https://doi.org/10.4043/27034-MS.

Woodroffe, S.A., Hill, J., Bustamante-Fernandez, E., Lloyd, J.M., Luff, J., Richards, S., Shennan, I., 2023. On the varied impact of the Storegga tsunami in Northwest Scotland. J. Quaternary Sci. https://doi.org/10.1002/jqs.3539.

Yhasnara, M., Costa, P., Dourado, F., Martins, M.V.A., Feist, L., Bellanova, P., Reicherter, K., 2023. Microtextural signatures in quartz grains and foraminifera from tsunami deposits of the Portuguese shelf. Geo-Mar. Lett. 43, 5. https://doi.org/10.1007/s00367-023-00747-0.

Yilmaz, O., 1987. Seismic Data Processing. Atlantic Books, Limited, Tulsa, Oklahoma.

Yoshii, T., Tanaka, S., Matsuyama, M., 2017. Tsunami deposits in a super-large wave flume. Mar. Geol. 391, 98–107. https://doi.org/10.1016/j.margeo.2017.07.020.